

# Ceramics International

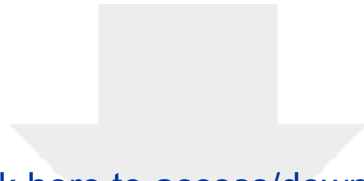
## Synthesis of nano Mg-Y/ZrO<sub>2</sub> ternary oxide eutectic system via co-precipitation method: Effects of calcination temperature --Manuscript Draft--

<b>Manuscript Number:</b>	CERI-D-22-03413R2
<b>Article Type:</b>	Full length article
<b>Keywords:</b>	Mg-Y/ZrO <sub>2</sub> ; Nano-powders; Co-precipitation; Crystallization degree; Particle dispersion
<b>Corresponding Author:</b>	jin chen kunming university of science and technology kunming, CHINA
<b>First Author:</b>	Hongju Qiu
<b>Order of Authors:</b>	Hongju Qiu Weiwei Huang Yanqiong Zhang jin chen Lei Gao Mamdouh Omran Nan Li Guo Chen
<b>Abstract:</b>	<p>In the family of inorganic nanomaterials, zirconia is a highly promising functional ceramic material with a high refractive index, excellent chemical inertness, high hardness, excellent thermal stability, and high dielectric constant. These properties are highlighted in nano-zirconia ceramics because nano-powders have a small particle size, dispersive distribution, decent morphology, and uniform distribution. In this paper, a co-precipitation process was proposed to prepare highly dispersed MgO-Y<sub>2</sub>O<sub>3</sub> co-stabilized ZrO<sub>2</sub> nano-powders, and the effects of different calcination temperatures on the crystallization degree and particle dispersion of zirconia nano-powders were studied by XRD, TG-DSC, Raman, FTIR, BET, TEM, and FEESM, respectively. The optimum conditions were obtained as follows: 6 hours of high-energy planetary grinding, calcination at 800°C in an electric furnace. With the optimum conditions, the average particle size of the prepared powder is 28.7 nm. The process is dedicated to enriching the research data on the controllable preparation of Mg-Y/ZrO<sub>2</sub> nano-powders using the co-precipitation method.</p>

**Declaration of interests**

The authors declare that they have no known competing financial interests or personal relationships that could have appeared to influence the work reported in this paper.

The authors declare the following financial interests/personal relationships which may be considered as potential competing interests:



Click here to access/download  
**e-component**  
Language Editing Certificate.pdf



1 Co-precipitation of nano Mg-Y/ZrO<sub>2</sub> ternary oxide eutectic system: Effects of  
2  
3 calcination temperature  
4  
5  
6  
7

8  
9 Hongju Qiu <sup>a</sup>, Weiwei Huang <sup>a</sup>, Yanqiong Zhang <sup>a</sup>, Jin Chen <sup>a, \*\*</sup>, Lei Gao <sup>a, \*\*</sup>,  
10  
11 Mamdouh Omran <sup>b</sup>, Li Nan<sup>c</sup>, Guo Chen <sup>a, \*</sup>  
12  
13  
14  
15  
16

17 <sup>a</sup> Kunming Key Laboratory of Energy Materials Chemistry, Yunnan Minzu University,  
18  
19 Kunming 650500, Yunnan, P.R. China.  
20  
21

22 <sup>b</sup> Process Metallurgy Research Group, Faculty of Technology, University of Oulu, Finland.  
23  
24

25 <sup>c</sup> College of Chemistry and Resources Engineering, Hong He University, Mengzi, China,  
26  
27 661199  
28  
29  
30  
31  
32

33  
34 \* Corresponding author: guochen@kust.edu.cn  
35

36  
37 \* Corresponding author: glkust2013@hotmail.com, jinchen@kust.edu.cn  
38  
39  
40  
41

42 **Abstract:** In the family of inorganic nanomaterials, zirconia is a highly promising functional ceramic  
43  
44 with a high refractive index, hardness, and dielectric constant, as well as excellent chemical inertness and  
45  
46 thermal stability. These properties are enhanced in nano-zirconia ceramics, because nanopowders have a  
47  
48 small particle size, good morphology, and uniform and dispersive distribution. In this study, a  
49  
50 co-precipitation process was proposed to synthesise highly dispersed MgO-Y<sub>2</sub>O<sub>3</sub> co-stabilized ZrO<sub>2</sub>  
51  
52  
53 nanopowders. The effects of different calcination temperatures on the crystallisation degree and particle  
54  
55  
56 dispersion of zirconia nanopowders were characterised by X-ray diffraction (XRD),  
57  
58  
59  
60  
61  
62  
63  
64  
65

1 thermogravimetry-differential scanning calorimetry (TG-DSC), Raman spectroscopy, Fourier transform  
2  
3 infrared spectroscopy (FTIR), nitrogen adsorption using the Brunauer–Emmett–Teller (BET) theory,  
4  
5  
6 transmission electron microscopy (TEM), and field emission scanning electron microscopy (FESEM). The  
7  
8  
9 optimum synthesis conditions were obtained as follows: 6 h of high-energy planetary grinding and  
10  
11 calcination at 800 °C in an electric furnace. Under these optimum conditions, the average particle size of  
12  
13 the prepared powder was 28.7 nm. This process enriches the literature on the controllable preparation of  
14  
15  
16  
17 Mg-Y/ZrO<sub>2</sub> nanopowders obtained by the co-precipitation method.

18  
19  
20 **Keywords:** Mg-Y/ZrO<sub>2</sub>; Nanopowders; Co-precipitation; Crystallisation degree; Particle dispersion;  
21  
22  
23  
24

## 25 **1. Introduction**

26  
27  
28 Zirconia is an important inorganic nonmetallic material with applications in ceramics, catalysts,  
29  
30 refractories, optics, aerospace, biology, and chemistry [1-4]. However, pure zirconia materials exhibit  
31  
32  
33  
34 volume change effects during the reversible martensitic transformation between the monoclinic phase and  
35  
36 tetragonal crystals, leading to a decline in their mechanical and thermal shock properties, which limits their  
37  
38  
39 application range [5-8].

40  
41  
42 To resolve this issue, studies have reported that the phase stability of pure zirconia materials may be  
43  
44 improved by co-doping zirconia with stabilisers, thus enhancing their mechanical properties and thermal  
45  
46 shock resistance [9-12]. Common stabilisers include oxides such as Y<sub>2</sub>O<sub>3</sub>, CaO, Al<sub>2</sub>O<sub>3</sub>, MgO, Sc<sub>2</sub>O, and  
47  
48  
49 CeO<sub>2</sub> [13-15]. The stable states of the zirconia materials generally include: tetragonal zirconia  
50  
51 polycrystalline (TZP), fully stabilized zirconia (FSZ), and partially stabilized zirconia (PSZ) [16]. Wen et al.  
52  
53 [17] investigated the improvement in the phase composition, packing density, microstructure, and  
54  
55  
56  
57  
58 compressive strength of MgO-PSZ ceramics by doping with a Y<sub>2</sub>O<sub>3</sub> stabiliser. The good performance of  
59  
60  
61  
62  
63  
64  
65

1 zirconia ceramics was reported to be owing to the ultrafine particle diameter and a reasonable proportion of  
2  
3 stabilisers. Abed et al. [18] explored the effect of the grain size of  $Y_2O_3$ - $ZrO_2$ - $MgAl_2O_4$  powders on the  
4  
5 properties of ceramic sintered bodies. The grain size greatly influenced the properties of zirconia ceramics,  
6  
7 in addition to the effect of stabiliser content. Therefore, the grain size and dispersion of the precursor  
8  
9 material are considered key factors in the preparation of high-toughness and high-strength zirconia  
10  
11 materials.  
12  
13  
14  
15  
16

17 Currently, the study of ultrafine nanoscale zirconia materials is attracting increasing attention [19,20].  
18  
19 Nanoparticles are solid particles with sizes in the range of 0.1–100 nm, between bulk materials and atoms  
20  
21 and molecules, and serve as the raw materials in nanotechnology [21]. Nanosystems have properties, such  
22  
23 as the small size, dielectric limit, and quantum tunnelling effects, which are not present in macroscopic  
24  
25 systems (with objects visible to the human eye as the lower limit) or mesoscopic systems (submicron level,  
26  
27 0.1–1  $\mu$ m). Therefore, nanosystems exhibit high catalytic activity and selectivity, high adsorption and  
28  
29 diffusion, and excellent optical properties (such as high transparency and magnetic properties), enhanced  
30  
31 toughness, lubricity, and other physical and chemical properties, which creates great potential for the  
32  
33 application of nanomaterials [22-24]. However, owing to the high surface energy of nanoparticles and van  
34  
35 der Waals forces between particles, nanoparticles are highly prone to agglomeration during preparation,  
36  
37 separation, storage, and application, which affects the advantages gained by the small size of these  
38  
39 materials. Therefore, maintaining good precursor dispersion and inhibiting nanoparticle agglomeration are  
40  
41 important research topics in nanotechnology [25,26].  
42  
43  
44  
45  
46  
47  
48  
49  
50  
51

52 Many methods are available for the preparation of nanoscale zirconia. Currently, wet chemical  
53  
54 preparation methods, such as hydrothermal [27], precipitation [28], sol-gel [29], microemulsion [30],  
55  
56 electrochemical synthesis [31], and solvent evaporation [32], are used. During chemical precipitation, a  
57  
58  
59  
60  
61  
62  
63  
64  
65

1 precipitant is added to a mixed solution to produce insoluble precipitates, such as hydroxides or sulfates.

2  
3 The precipitates serve as the raw precursors. After the subsequent washing-filtering-heating process,  
4  
5  
6 precursors decompose into powder products. Chemical precipitation [33] is often selected for the  
7  
8  
9 preparation of powder products at the laboratory scale because of its low reactant count and equipment  
10  
11 requirements, ease of operation, and high product purity. To prepare nanopowders, including multiple  
12  
13  
14 oxides, the chemical method of co-precipitation is widely used [34,35].  
15

16  
17 Co-precipitation has been successfully applied to the preparation of nanoscale zirconia. Santoyo et al.  
18  
19  
20 [36] used this method to obtain nanoscale tetragonal-phase zirconia. Yttrium oxide (3 mol%) partially  
21  
22 stabilised zirconia particles were dissolved in an  $\text{Al}(\text{NO}_3)_3 \cdot 9\text{H}_2\text{O}$  solution and subsequently co-precipitated  
23  
24  
25 with ammonia to obtain 3 mol% YSZ- $\text{Al}_2\text{O}_3$  particles (the target precursor). The target precursor was  
26  
27  
28 washed with ultrapure water and anhydrous ethanol, followed by drying in an oven at 90 °C. Subsequently,  
29  
30  
31 the precursor sample was calcined at 300 °C for 20 h to obtain  $\text{Al}_2\text{O}_3$  and  $\text{Y}_2\text{O}_3$  stabilized zirconium  
32  
33  
34 dioxide nanopowders. The cold pressed nanopowders were sintered in air at 1100 °C for 6 h to obtain  
35  
36  
37 YSZ- $\text{Al}_2\text{O}_3$  ceramics. Hsu et al. [37] obtained tetragonal-phase  $\text{ZrO}_2$  with a size of 21.3 nm using the  
38  
39  
40 co-precipitation method.

41  
42 In this study, a co-precipitation process is proposed to prepare highly dispersed yttrium oxide and  
43  
44  
45 magnesium oxide-stabilised zirconium oxide nanopowders.  $\text{ZrOCl}_2 \cdot 8\text{H}_2\text{O}$  is used as the zirconium source  
46  
47  
48 mixed with  $\text{Y}(\text{NO}_3)_3 \cdot 6\text{H}_2\text{O}$  and  $\text{MgCl}_2 \cdot 6\text{H}_2\text{O}$ . The mixture is co-precipitated by titration with  $\text{NH}_3 \cdot \text{H}_2\text{O}$   
49  
50  
51 under high-speed stirring, and nanoscale zirconium oxide powder is produced after extraction and  
52  
53  
54 subsequent washing, ball milling, drying, and calcination. The obtained samples are characterised by  
55  
56  
57 thermogravimetry-differential scanning calorimetry (TG-DSC), X-ray diffraction (XRD), Raman  
58  
59  
60 spectroscopy, Fourier transform infrared spectroscopy (FTIR), nitrogen adsorption using the Brunauer–  
61  
62  
63  
64  
65

1 Emmett–Teller (BET) theory, transmission electron microscopy (TEM), and field emission scanning  
2  
3 electron microscopy (FESEM). The effects of the calcination temperature on the degree of crystallisation,  
4  
5 physical phase composition, and particle dispersion of the final tetragonal-phase Mg-Y/ZrO<sub>2</sub> (*t*-Mg-Y/ZrO<sub>2</sub>)  
6  
7 are investigated.  
8  
9

## 10 11 12 13 14 **2. Experiments**

### 15 16 17 **2.1 Materials**

18  
19 The chemicals used in the experimental process are listed in Table 1, and the apparatus and equipment  
20  
21 used are listed in Table 2.  
22  
23

### 24 25 **2.2 Preparation of Mg-Y/ZrO<sub>2</sub> nanoparticles**

26  
27 Firstly, 0.002 mol Y(NO<sub>3</sub>)<sub>3</sub>·6H<sub>2</sub>O, 0.006 mol MgCl<sub>2</sub>·6H<sub>2</sub>O, and 0.092 mol ZrOCl<sub>2</sub>·8H<sub>2</sub>O were  
28  
29 accurately weighed using an analytical balance and mixed to prepare a 0.1 mol/L sample solution.  
30  
31 Subsequently, 150 mL of a 25–28 % ammonia solution was diluted to prepare a 2 mol/L ammonia solution  
32  
33 using a measuring cylinder (sealed with cling film to prevent ammonia evaporation). For the precipitation  
34  
35 process, the 2 mol/L dilute ammonia solution was added dropwise to the sample solution under high-speed  
36  
37 magnetic stirring. The pH at the end of the titration was controlled to 10 to ensure complete precipitation of  
38  
39 Zr<sup>4+</sup>, Mg<sup>2+</sup> and Y<sup>3+</sup>. After aging, the sample was washed four times with 0.15 mol/L dilute ammonia  
40  
41 solution, and then washed once with anhydrous ethanol. The last washing solution was tested for the  
42  
43 absence of white Cl<sup>-</sup> precipitation using a 0.1000 mol/L AgNO<sub>3</sub> solution. The washed samples were then  
44  
45 dispersed in an anhydrous ethanol medium, subjected to high-energy planetary ball milling (for 6 h), and  
46  
47 subsequently dried. The dried powder was finely ground in a grinding pot and passed through an 80-mesh  
48  
49 sieve. Calcination was performed in a medium-ring electric furnace using specially designed temperatures  
50  
51  
52  
53  
54  
55  
56  
57  
58  
59  
60  
61  
62  
63  
64  
65

1 (200–800 °C). Subsequently, the calcined powder was passed through a 200-mesh sieve. The  
2  
3  
4  
5  
6  
7  
8  
9  
10  
11  
12  
13  
14  
15  
16  
17  
18  
19  
20  
21  
22  
23  
24  
25  
26  
27  
28  
29  
30  
31  
32  
33  
34  
35  
36  
37  
38  
39  
40  
41  
42  
43  
44  
45  
46  
47  
48  
49  
50  
51  
52  
53  
54  
55  
56  
57  
58  
59  
60  
61  
62  
63  
64  
65

(200–800 °C). Subsequently, the calcined powder was passed through a 200-mesh sieve. The  
aforementioned well-designed experimental procedure was used to investigate the optimum conditions for  
the preparation of highly dispersed, high-quality *t*-Mg-Y/ZrO<sub>2</sub> nanopowder materials (as shown in Fig. 1).

### 2.3 Characterisation of as-prepared Mg-Y/ZrO<sub>2</sub> nanoparticles

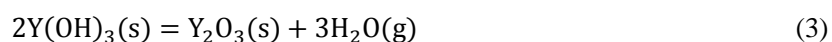
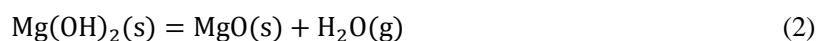
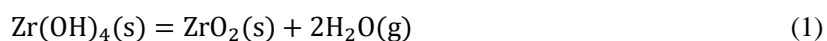
The crystalline phase composition of zirconia nanopowders is a key factor in characterising their  
properties. In this study, a thermal gravimetric analyser (TGA) was used to measure the change in material  
mass with temperature (and time) to observe the quantitative and qualitative variations in temperature  
during the generation of zirconia powders from their precursors, and thus analyse the thermal stability of  
the material. The powder samples were qualitatively characterised by XRD, and the crystallinity of these  
samples was analysed (scanning speed of 5 °/min). Furthermore, XRD results were analysed using Jade  
software and Scherrer's equation to calculate the zirconia grain size. The molecular vibration of the samples  
was characterised by Raman spectroscopy. The powder surface adsorption energy and pore size variation  
were characterized by nitrogen adsorption using the BET theory. A combination of FTIR with computer  
technology was used to characterise the chemical structure of the surface of the powder particles using  
interferograms, in a test spectrum range of 500–4000 cm<sup>-1</sup>. The FESEM instrument had a ultra-high  
resolution that was used to magnify zirconia nanopowders in a low-vacuum environment to monitor the  
microscopic morphology of the sample.

## 3. Results and discussion

### 3.1 TG-DSC characterisation

Characterisation by TG-DSC was used to obtain the weight loss of the sample during the heating  
process, and it was further used to characterise the changes in the precursor at different temperature stages.

1 The atmosphere used for TG-DSC analysis was air, the ramp rate was 5 °C/min, and the test temperature  
2  
3 range was 18–900 °C. Figure 2 shows the TG-DSC curve of the precursor samples, which initially  
4  
5 decreased rapidly and then gradually flattened. This was mainly owing to the loss of a large quantity of free  
6  
7 and bound water from the precursor, with a total burn loss of 15.03 %. The DSC curve shows two thermal  
8  
9 absorption peaks at 70 and 165 °C, combined with the TG and differential thermogravimetry (DTG) curves.  
10  
11 The thermal absorption peak at 70 °C was attributed to the loss of adsorbed and bound water, while the  
12  
13 thermal absorption peak at 165 °C was associated with the dehydrative decomposition of zirconium,  
14  
15 magnesium, and yttrium hydroxides during their transformations to ZrO<sub>2</sub>, MgO<sub>2</sub> and Y<sub>2</sub>O<sub>3</sub> as follows:  
16  
17  
18  
19  
20  
21



25  
26  
27  
28  
29  
30  
31 Additionally, two exothermic peaks were observed at 292 and 500 °C in the DSC curves. The peak at  
32  
33 292 °C was weak because the transformation of amorphous zirconia was in the initial stage. Furthermore,  
34  
35 the peak at 500 °C was extremely strong, but the corresponding weight loss in the TG and DTG curves was  
36  
37 absent. This result was because of the specific chemical reactions that caused the exothermic peaks by  
38  
39 generating large amounts of heat, which had an important effect on the crystallisation of zirconia  
40  
41  
42  
43  
44  
45  
46  
47  
48  
49  
50  
51  
52  
53  
54  
55  
56  
57  
58  
59  
60  
61  
62  
63  
64  
65  
66  
67  
68  
69  
70  
71  
72  
73  
74  
75  
76  
77  
78  
79  
80  
81  
82  
83  
84  
85  
86  
87  
88  
89  
90  
91  
92  
93  
94  
95  
96  
97  
98  
99  
100  
101  
102  
103  
104  
105  
106  
107  
108  
109  
110  
111  
112  
113  
114  
115  
116  
117  
118  
119  
120  
121  
122  
123  
124  
125  
126  
127  
128  
129  
130  
131  
132  
133  
134  
135  
136  
137  
138  
139  
140  
141  
142  
143  
144  
145  
146  
147  
148  
149  
150  
151  
152  
153  
154  
155  
156  
157  
158  
159  
160  
161  
162  
163  
164  
165  
166  
167  
168  
169  
170  
171  
172  
173  
174  
175  
176  
177  
178  
179  
180  
181  
182  
183  
184  
185  
186  
187  
188  
189  
190  
191  
192  
193  
194  
195  
196  
197  
198  
199  
200  
201  
202  
203  
204  
205  
206  
207  
208  
209  
210  
211  
212  
213  
214  
215  
216  
217  
218  
219  
220  
221  
222  
223  
224  
225  
226  
227  
228  
229  
230  
231  
232  
233  
234  
235  
236  
237  
238  
239  
240  
241  
242  
243  
244  
245  
246  
247  
248  
249  
250  
251  
252  
253  
254  
255  
256  
257  
258  
259  
260  
261  
262  
263  
264  
265  
266  
267  
268  
269  
270  
271  
272  
273  
274  
275  
276  
277  
278  
279  
280  
281  
282  
283  
284  
285  
286  
287  
288  
289  
290  
291  
292  
293  
294  
295  
296  
297  
298  
299  
300  
301  
302  
303  
304  
305  
306  
307  
308  
309  
310  
311  
312  
313  
314  
315  
316  
317  
318  
319  
320  
321  
322  
323  
324  
325  
326  
327  
328  
329  
330  
331  
332  
333  
334  
335  
336  
337  
338  
339  
340  
341  
342  
343  
344  
345  
346  
347  
348  
349  
350  
351  
352  
353  
354  
355  
356  
357  
358  
359  
360  
361  
362  
363  
364  
365  
366  
367  
368  
369  
370  
371  
372  
373  
374  
375  
376  
377  
378  
379  
380  
381  
382  
383  
384  
385  
386  
387  
388  
389  
390  
391  
392  
393  
394  
395  
396  
397  
398  
399  
400  
401  
402  
403  
404  
405  
406  
407  
408  
409  
410  
411  
412  
413  
414  
415  
416  
417  
418  
419  
420  
421  
422  
423  
424  
425  
426  
427  
428  
429  
430  
431  
432  
433  
434  
435  
436  
437  
438  
439  
440  
441  
442  
443  
444  
445  
446  
447  
448  
449  
450  
451  
452  
453  
454  
455  
456  
457  
458  
459  
460  
461  
462  
463  
464  
465  
466  
467  
468  
469  
470  
471  
472  
473  
474  
475  
476  
477  
478  
479  
480  
481  
482  
483  
484  
485  
486  
487  
488  
489  
490  
491  
492  
493  
494  
495  
496  
497  
498  
499  
500  
501  
502  
503  
504  
505  
506  
507  
508  
509  
510  
511  
512  
513  
514  
515  
516  
517  
518  
519  
520  
521  
522  
523  
524  
525  
526  
527  
528  
529  
530  
531  
532  
533  
534  
535  
536  
537  
538  
539  
540  
541  
542  
543  
544  
545  
546  
547  
548  
549  
550  
551  
552  
553  
554  
555  
556  
557  
558  
559  
560  
561  
562  
563  
564  
565  
566  
567  
568  
569  
570  
571  
572  
573  
574  
575  
576  
577  
578  
579  
580  
581  
582  
583  
584  
585  
586  
587  
588  
589  
590  
591  
592  
593  
594  
595  
596  
597  
598  
599  
600  
601  
602  
603  
604  
605  
606  
607  
608  
609  
610  
611  
612  
613  
614  
615  
616  
617  
618  
619  
620  
621  
622  
623  
624  
625  
626  
627  
628  
629  
630  
631  
632  
633  
634  
635  
636  
637  
638  
639  
640  
641  
642  
643  
644  
645  
646  
647  
648  
649  
650  
651  
652  
653  
654  
655  
656  
657  
658  
659  
660  
661  
662  
663  
664  
665  
666  
667  
668  
669  
670  
671  
672  
673  
674  
675  
676  
677  
678  
679  
680  
681  
682  
683  
684  
685  
686  
687  
688  
689  
690  
691  
692  
693  
694  
695  
696  
697  
698  
699  
700  
701  
702  
703  
704  
705  
706  
707  
708  
709  
710  
711  
712  
713  
714  
715  
716  
717  
718  
719  
720  
721  
722  
723  
724  
725  
726  
727  
728  
729  
730  
731  
732  
733  
734  
735  
736  
737  
738  
739  
740  
741  
742  
743  
744  
745  
746  
747  
748  
749  
750  
751  
752  
753  
754  
755  
756  
757  
758  
759  
760  
761  
762  
763  
764  
765  
766  
767  
768  
769  
770  
771  
772  
773  
774  
775  
776  
777  
778  
779  
780  
781  
782  
783  
784  
785  
786  
787  
788  
789  
790  
791  
792  
793  
794  
795  
796  
797  
798  
799  
800  
801  
802  
803  
804  
805  
806  
807  
808  
809  
810  
811  
812  
813  
814  
815  
816  
817  
818  
819  
820  
821  
822  
823  
824  
825  
826  
827  
828  
829  
830  
831  
832  
833  
834  
835  
836  
837  
838  
839  
840  
841  
842  
843  
844  
845  
846  
847  
848  
849  
850  
851  
852  
853  
854  
855  
856  
857  
858  
859  
860  
861  
862  
863  
864  
865  
866  
867  
868  
869  
870  
871  
872  
873  
874  
875  
876  
877  
878  
879  
880  
881  
882  
883  
884  
885  
886  
887  
888  
889  
890  
891  
892  
893  
894  
895  
896  
897  
898  
899  
900  
901  
902  
903  
904  
905  
906  
907  
908  
909  
910  
911  
912  
913  
914  
915  
916  
917  
918  
919  
920  
921  
922  
923  
924  
925  
926  
927  
928  
929  
930  
931  
932  
933  
934  
935  
936  
937  
938  
939  
940  
941  
942  
943  
944  
945  
946  
947  
948  
949  
950  
951  
952  
953  
954  
955  
956  
957  
958  
959  
960  
961  
962  
963  
964  
965  
966  
967  
968  
969  
970  
971  
972  
973  
974  
975  
976  
977  
978  
979  
980  
981  
982  
983  
984  
985  
986  
987  
988  
989  
990  
991  
992  
993  
994  
995  
996  
997  
998  
999  
1000

### 3.2 XRD characterisation

50 To further investigate the phase transformation process, XRD analysis was used to characterise the  
51  
52 phases of the precursors and samples calcined at temperatures of at 200–800 °C for 2 h. Figure 3 shows the  
53  
54 scanned XRD spectra of the precursor and zirconia powders prepared at varying calcination temperatures.  
55  
56  
57  
58  
59  
60  
61  
62  
63  
64  
65  
66  
67  
68  
69  
70  
71  
72  
73  
74  
75  
76  
77  
78  
79  
80  
81  
82  
83  
84  
85  
86  
87  
88  
89  
90  
91  
92  
93  
94  
95  
96  
97  
98  
99  
100  
101  
102  
103  
104  
105  
106  
107  
108  
109  
110  
111  
112  
113  
114  
115  
116  
117  
118  
119  
120  
121  
122  
123  
124  
125  
126  
127  
128  
129  
130  
131  
132  
133  
134  
135  
136  
137  
138  
139  
140  
141  
142  
143  
144  
145  
146  
147  
148  
149  
150  
151  
152  
153  
154  
155  
156  
157  
158  
159  
160  
161  
162  
163  
164  
165  
166  
167  
168  
169  
170  
171  
172  
173  
174  
175  
176  
177  
178  
179  
180  
181  
182  
183  
184  
185  
186  
187  
188  
189  
190  
191  
192  
193  
194  
195  
196  
197  
198  
199  
200  
201  
202  
203  
204  
205  
206  
207  
208  
209  
210  
211  
212  
213  
214  
215  
216  
217  
218  
219  
220  
221  
222  
223  
224  
225  
226  
227  
228  
229  
230  
231  
232  
233  
234  
235  
236  
237  
238  
239  
240  
241  
242  
243  
244  
245  
246  
247  
248  
249  
250  
251  
252  
253  
254  
255  
256  
257  
258  
259  
260  
261  
262  
263  
264  
265  
266  
267  
268  
269  
270  
271  
272  
273  
274  
275  
276  
277  
278  
279  
280  
281  
282  
283  
284  
285  
286  
287  
288  
289  
290  
291  
292  
293  
294  
295  
296  
297  
298  
299  
300  
301  
302  
303  
304  
305  
306  
307  
308  
309  
310  
311  
312  
313  
314  
315  
316  
317  
318  
319  
320  
321  
322  
323  
324  
325  
326  
327  
328  
329  
330  
331  
332  
333  
334  
335  
336  
337  
338  
339  
340  
341  
342  
343  
344  
345  
346  
347  
348  
349  
350  
351  
352  
353  
354  
355  
356  
357  
358  
359  
360  
361  
362  
363  
364  
365  
366  
367  
368  
369  
370  
371  
372  
373  
374  
375  
376  
377  
378  
379  
380  
381  
382  
383  
384  
385  
386  
387  
388  
389  
390  
391  
392  
393  
394  
395  
396  
397  
398  
399  
400  
401  
402  
403  
404  
405  
406  
407  
408  
409  
410  
411  
412  
413  
414  
415  
416  
417  
418  
419  
420  
421  
422  
423  
424  
425  
426  
427  
428  
429  
430  
431  
432  
433  
434  
435  
436  
437  
438  
439  
440  
441  
442  
443  
444  
445  
446  
447  
448  
449  
450  
451  
452  
453  
454  
455  
456  
457  
458  
459  
460  
461  
462  
463  
464  
465  
466  
467  
468  
469  
470  
471  
472  
473  
474  
475  
476  
477  
478  
479  
480  
481  
482  
483  
484  
485  
486  
487  
488  
489  
490  
491  
492  
493  
494  
495  
496  
497  
498  
499  
500  
501  
502  
503  
504  
505  
506  
507  
508  
509  
510  
511  
512  
513  
514  
515  
516  
517  
518  
519  
520  
521  
522  
523  
524  
525  
526  
527  
528  
529  
530  
531  
532  
533  
534  
535  
536  
537  
538  
539  
540  
541  
542  
543  
544  
545  
546  
547  
548  
549  
550  
551  
552  
553  
554  
555  
556  
557  
558  
559  
560  
561  
562  
563  
564  
565  
566  
567  
568  
569  
570  
571  
572  
573  
574  
575  
576  
577  
578  
579  
580  
581  
582  
583  
584  
585  
586  
587  
588  
589  
590  
591  
592  
593  
594  
595  
596  
597  
598  
599  
600  
601  
602  
603  
604  
605  
606  
607  
608  
609  
610  
611  
612  
613  
614  
615  
616  
617  
618  
619  
620  
621  
622  
623  
624  
625  
626  
627  
628  
629  
630  
631  
632  
633  
634  
635  
636  
637  
638  
639  
640  
641  
642  
643  
644  
645  
646  
647  
648  
649  
650  
651  
652  
653  
654  
655  
656  
657  
658  
659  
660  
661  
662  
663  
664  
665  
666  
667  
668  
669  
670  
671  
672  
673  
674  
675  
676  
677  
678  
679  
680  
681  
682  
683  
684  
685  
686  
687  
688  
689  
690  
691  
692  
693  
694  
695  
696  
697  
698  
699  
700  
701  
702  
703  
704  
705  
706  
707  
708  
709  
710  
711  
712  
713  
714  
715  
716  
717  
718  
719  
720  
721  
722  
723  
724  
725  
726  
727  
728  
729  
730  
731  
732  
733  
734  
735  
736  
737  
738  
739  
740  
741  
742  
743  
744  
745  
746  
747  
748  
749  
750  
751  
752  
753  
754  
755  
756  
757  
758  
759  
760  
761  
762  
763  
764  
765  
766  
767  
768  
769  
770  
771  
772  
773  
774  
775  
776  
777  
778  
779  
780  
781  
782  
783  
784  
785  
786  
787  
788  
789  
790  
791  
792  
793  
794  
795  
796  
797  
798  
799  
800  
801  
802  
803  
804  
805  
806  
807  
808  
809  
810  
811  
812  
813  
814  
815  
816  
817  
818  
819  
820  
821  
822  
823  
824  
825  
826  
827  
828  
829  
830  
831  
832  
833  
834  
835  
836  
837  
838  
839  
840  
841  
842  
843  
844  
845  
846  
847  
848  
849  
850  
851  
852  
853  
854  
855  
856  
857  
858  
859  
860  
861  
862  
863  
864  
865  
866  
867  
868  
869  
870  
871  
872  
873  
874  
875  
876  
877  
878  
879  
880  
881  
882  
883  
884  
885  
886  
887  
888  
889  
890  
891  
892  
893  
894  
895  
896  
897  
898  
899  
900  
901  
902  
903  
904  
905  
906  
907  
908  
909  
910  
911  
912  
913  
914  
915  
916  
917  
918  
919  
920  
921  
922  
923  
924  
925  
926  
927  
928  
929  
930  
931  
932  
933  
934  
935  
936  
937  
938  
939  
940  
941  
942  
943  
944  
945  
946  
947  
948  
949  
950  
951  
952  
953  
954  
955  
956  
957  
958  
959  
960  
961  
962  
963  
964  
965  
966  
967  
968  
969  
970  
971  
972  
973  
974  
975  
976  
977  
978  
979  
980  
981  
982  
983  
984  
985  
986  
987  
988  
989  
990  
991  
992  
993  
994  
995  
996  
997  
998  
999  
1000

1 characteristic peaks for the tetragonal zirconia phase ( $t\text{-ZrO}_2$ ) were observed when the sample was calcined  
2  
3 at 400 °C, the  $t\text{-ZrO}_2$  diffraction peak became more intense, and its crystallisation was favored when the  
4  
5 sample was calcined at 800 °C. The average grain sizes calculated using Scherrer's equation were 18.6,  
6  
7 23.3, and 28.7 nm for samples calcined at temperatures of 400–800 °C, respectively, which indicated that  
8  
9 the calcination temperature was positively correlated with the grain size of the powders. In finding the  
10  
11 average particle size, XRD data from large angle diffraction was used, taking the strongest and most stable  
12  
13 diffraction peaks where they can be found. However, the peaks were sharper and had smaller full widths at  
14  
15 half maxima (FWHMs) as the calcination temperature increased, and the best crystallinity for the zirconia  
16  
17 powder sample was observed at 800 °C.  
18  
19  
20  
21  
22  
23  
24

### 25 **3.3 Raman characterisation**

26  
27 Raman spectroscopy is an effective way to distinguish the zirconia crystalline form. The tetragonal  
28  
29 phase of zirconia has six Raman active vibrational modes ( $A_{1g}+2B_{1g}+3E_g$ ):  $A_{1g}^+$ : 600  $\text{cm}^{-1}$  (very weak),  $B_{1g}$ :  
30  
31 147 and 315  $\text{cm}^{-1}$ ,  $E_g$ : 269, 459, and 643  $\text{cm}^{-1}$ . Theoretically, the cubic phase has only one Raman active  
32  
33 vibrational mode, typically observed as a broad spectral peak from 530 to 670  $\text{cm}^{-1}$  [38]. The monoclinic  
34  
35 phase has 18 Raman active vibrational modes: ( $9A_g+9B_g$ ) and the following vibration spectral peaks can  
36  
37 generally be observed:  $A_g$ : 176, 187, 300, 475, 558, 635, and 760  $\text{cm}^{-1}$ ,  $B_g$ : 220, 333, 344, 380, 510, 536,  
38  
39 and 613  $\text{cm}^{-1}$ . For further differentiation, Raman spectroscopy was performed on the obtained zirconia  
40  
41 nanoparticle samples, and Raman spectra are shown in Fig. 4(a). The zirconia samples showed a small  
42  
43 number of weak vibrational peaks associated with the monoclinic phase, while vibrational peaks  
44  
45 corresponding to the tetragonal phase were observed at 146, 260, 318, 464, and 642  $\text{cm}^{-1}$ , and no broad  
46  
47 peaks were observed in the cubic phase wavelength range of 530–670  $\text{cm}^{-1}$ . Thus, it was confirmed that the  
48  
49 obtained Mg-Y/ZrO<sub>2</sub> nanoparticles were mixed crystals with a large amount of the tetragonal zirconia  
50  
51  
52  
53  
54  
55  
56  
57  
58  
59  
60  
61  
62  
63  
64  
65

1 phase and a small of the monoclinic zirconia ( $m\text{-ZrO}_2$ ) phase. Moreover, the  $t\text{-ZrO}_2$  phase vibrational peak  
2  
3 intensity gradually showed a positive relationship with the calcination temperature, which further  
4  
5 confirmed that the crystallinity of the sample reached a maximum after calcination at 800 °C, where the  
6  
7 transformation from the amorphous phase to the tetragonal phase was nearly complete.  
8  
9

10  
11 The original Raman spectra were fitted with multiple Gaussian peaks using the Origin software. The  
12  
13 relationship between the calcination temperature and crystalline phase composition of the powders was  
14  
15 investigated in detail based on characteristic spectral information, such as the position, intensity, area, and  
16  
17 FWHM of the Gaussian peaks. Figures 4(b)–(d) show the fitted curves of Raman spectra for samples  
18  
19 calcined at temperatures of 400–800 °C, respectively. With increasing calcination temperature, the peak  
20  
21 areas of the characteristic Raman peak positions gradually increased, whereas the FWHM gradually  
22  
23 decreased. Furthermore, since crystallinity is negatively correlated with FWHM, it was concluded that  
24  
25 crystallinity gradually increased with increasing calcination temperature. Moreover, maintaining the  
26  
27 precursor at a calcination temperature of 800 °C for 2 h was sufficient to achieve the best crystallinity in  
28  
29 this study. The Raman results were consistent with the XRD results.  
30  
31  
32  
33  
34  
35  
36  
37  
38

### 39 **3.4 FTIR characterization**

40  
41 The effects of co-doping magnesium and yttrium on the surface chemical structure of zirconia  
42  
43 powders were investigated by FTIR measurements of samples prepared at various calcination temperatures.  
44  
45 As shown in the first red curve of Fig. 5, five characteristic FTIR peaks were detected in the prepared  
46  
47 precursor powders at 3411.67, 1590.48, 1352.05, 1063.86, and 422.30  $\text{cm}^{-1}$ . Specifically, the characteristic  
48  
49 absorption peaks of Zr-O, Zr=O, and Zr-O-Zr bonds appeared at wavelengths of 1352.05, 1063.86, and  
50  
51 600–650  $\text{cm}^{-1}$ , respectively, which confirmed the presence of zirconia. Highly pure water was used as the  
52  
53 medium in the co-precipitation experiments; therefore, strong Zr-OH and O-H vibrational absorption peaks  
54  
55  
56  
57  
58  
59  
60  
61  
62  
63  
64  
65

1 were observed at 3411.67 and 1590.48  $\text{cm}^{-1}$ , respectively. Thus, the hydrophilic nature of the O-H bond  
2  
3 facilitated the dispersion of zirconium oxide in water during the preparation process. Because no surface  
4  
5 modifier was added during the preparation process, no other peaks were present in the FTIR spectrum of  
6  
7 the precursors.  
8  
9

10  
11 Furthermore, based on the FTIR spectra of the precursor and powders prepared at calcination  
12  
13 temperatures of 200–800  $^{\circ}\text{C}$ , it was possible to compare the characteristic peak at 422.30  $\text{cm}^{-1}$ , which  
14  
15 increased and shifted to a higher wavelength with a Doppler shift (blue shift) with increasing calcination  
16  
17 temperature. This phenomenon was explained by the exchange of heat with an increase in calcination  
18  
19 temperature, which led to a phase transformation to form crystalline particles, followed by the formation of  
20  
21 the pure tetragonal phase in the final calcined Mg-Y/ZrO<sub>2</sub> sample.  
22  
23  
24  
25  
26

### 27 **3.5 BET characterisation**

28  
29 A specific surface area tester was used to analyse the nitrogen adsorption-desorption curves. Powder  
30  
31 samples were dried at a constant temperature of 150  $^{\circ}\text{C}$  for 6 h and tested at -196  $^{\circ}\text{C}$  in liquid nitrogen  
32  
33 atmosphere. The pore size distribution (PSD) curves of the powder samples were calculated using the  
34  
35 Barrett–Joyner–Halenda (BJH) algorithm, and the specific surface areas of the powder samples were  
36  
37 obtained using the BET algorithm.  
38  
39  
40  
41  
42  
43

44  
45 Figure 6 shows the nitrogen adsorption-desorption curves and PSD curves for the precursors and  
46  
47 powder samples calcined at temperatures of 200–800  $^{\circ}\text{C}$ . Figure 6(a) shows that the adsorption-desorption  
48  
49 curves of the precursor calcined at temperatures of 200 and 400  $^{\circ}\text{C}$  had a distinct inflection (point A) at low  
50  
51  $P/P_0$ , which is the initial steep region of the isotherm. Inflection point A indicates that the adsorption  
52  
53 corresponding to the monolayer reached the maximum saturation adsorption capacity. The second  
54  
55 molecular layer started to accumulate by adsorption as the relative pressure increased. At the saturated  
56  
57  
58  
59  
60  
61  
62  
63  
64  
65

1 vapour pressure, the number of adsorbed molecular layers is unlimited; thus, these powder samples  
2  
3 exhibited a type II isotherm (also called type S). In contrast, the adsorption-desorption isotherms of powder  
4  
5 samplers calcines at a temperature of 600 and 800 °C exhibited the typical type IV isotherm, which curves  
6  
7 convexly upwards in the low  $P/P_0$  region. Conversely, in the higher  $P/P_0$  region, the isotherm increases  
8  
9 sharply because of capillary coalescence of the adsorbate. Subsequently, adsorption occurs only on the  
10  
11 external surface, and the curve becomes flat when all the pores coalesce. At relative pressures close to 1,  
12  
13 adsorption occurs on the larger pores and the curve increases. Because of the occurrence of capillary  
14  
15 coalescence, hysteresis is observed in the area, and the isotherm obtained during desorption disagrees with  
16  
17 the adsorption branch of the isotherm. The former isotherm is higher, producing an adsorption hysteresis,  
18  
19 which causes the back-lag cycle. According to the latest IUPAC classification, the saturation adsorption  
20  
21 plateau of the H3 type hysteresis loop was absent in the isotherm of the powder sample calcined at a  
22  
23 temperature of 600 °C, which indicated a remarkably irregular pore structure. The H2 type hysteresis loop  
24  
25 observed for the powder sample prepared at a calcination temperature of 800 °C had a saturation adsorption  
26  
27 plateau in the isotherm, which indicated a more uniform pore size distribution.

28  
29 The PSD curves shown in Fig. 6(b) indicate that the most accessible pore size was 12.216 nm, which  
30  
31 was observed for the powder sample prepared at a calcination temperature of 800 °C. The BET analysis  
32  
33 showed that the specific surface area of zirconia nanopowders has a negative relationship with the  
34  
35 calcination temperature, the minimum particle size was received at the calcined temperature of 200 °C.  
36  
37 However, we have noticed that hard agglomerates were formed in the sample prepared with a calcined  
38  
39 temperature of 200 °C because of the great surface activity of the sample. Whilst, samples calcined at  
40  
41 800 °C have a specific surface area of 13.249 m<sup>2</sup>/g, leading to a more uniform particle size distribution,  
42  
43  
44  
45  
46  
47  
48  
49  
50  
51  
52  
53  
54  
55  
56  
57  
58  
59  
60  
61  
62  
63  
64  
65

1 high sphericity, and lower surface energy, which makes them more favorable for subsequent applications  
2  
3 [39-42].  
4  
5

### 6 **3.6 SEM characterization**

7

8 The SEM results showed the distribution and morphology of zirconia clusters. Samples were tested by  
9 dropping a 50 wt.% mass fraction of the zirconia cluster dispersion onto a silicon wafer, followed by drying  
10 under ambient conditions. Before SEM analysis, the samples were subjected to gold plating to impart  
11 electrical conductivity.  
12  
13  
14  
15  
16  
17  
18

19 Figures 7(a)–(d) show the SEM images of the Mg-Y/ZrO<sub>2</sub> nanoparticles obtained by calcination at  
20 temperatures of 200–800 °C, at 200 000 times magnification using high-magnification electron microscopy.  
21  
22 A comparison of the four SEM micrographs shows that the calcination temperature was positively  
23 correlated with the nano-zirconia particle diameter. The nano Mg-Y/ZrO<sub>2</sub> powder particles prepared at a  
24 calcination temperature of 200 °C were small but irregularly arranged, and intermolecular forces led to  
25 distinct agglomeration. At calcination temperatures of 400–600 °C, the nano Mg-Y/ZrO<sub>2</sub> powder particles  
26 grew in size gradually, and the quasi-spherical morphology was gradually enhanced. At a calcination  
27 temperature of 800 °C, particle agglomeration was absent in the prepared nano Mg-Y/ZrO<sub>2</sub> powder, and the  
28 particle morphology was sphere-like with a more uniform particle distribution (shown in Fig. 7(d)).  
29  
30  
31  
32  
33  
34  
35  
36  
37  
38  
39  
40  
41  
42  
43  
44  
45  
46  
47  
48  
49  
50  
51  
52  
53  
54  
55  
56  
57  
58  
59  
60  
61  
62  
63  
64  
65

### 66 **4. Conclusion**

67 In this study, a co-precipitation process was proposed to synthesise Mg-Y/ZrO<sub>2</sub> nanopowders with a  
68 regular spherical morphology, good crystallisation, uniform distribution, and ultrafine diameter. The  
69  
70  
71  
72  
73  
74  
75

1 obtained samples were characterised by TG-DSC, XRD, Raman, FTIR, nitrogen adsorption using BET  
2  
3 theory, TEM, and FESEM. The main conclusions are as follows:  
4

5  
6 (1) Effect of calcination temperature on crystallinity: Both the precursors and the samples calcined at  
7  
8 200 °C were amorphous. The transformation of the precursor was initiated at a calcination temperature of  
9  
10 292 °C. The characteristic peaks of the tetragonal zirconia phase were observed at calcination temperatures  
11  
12 of 500 °C; the tetragonal zirconia diffraction peak increased and its crystallisation was favoured at a  
13  
14 calcination temperature of 800 °C.  
15  
16  
17

18  
19 (2) Effect of calcination temperature on dispersibility: The specific surface area of the Mg-Y/ZrO<sub>2</sub>  
20  
21 nanoparticles was negatively correlated with calcination temperature. The elevated heat reduced the surface  
22  
23 energy of the nano-zirconia powder, and consequently resulted in a good powder dispersion.  
24  
25  
26

27  
28 (3) The optimised synthesis conditions for the preparation of Mg-Y/ZrO<sub>2</sub> nanopowders were: 6 h of  
29  
30 high-energy planetary grinding, calcination at 800 °C in an electric furnace. Under optimum conditions, the  
31  
32 average diameter of the prepared particles was 28.7 nm. The process will enrich the research data in  
33  
34 literature on the controllable preparation of MgO-Y<sub>2</sub>O<sub>3</sub> co-stabilized ZrO<sub>2</sub> nanopowders using the  
35  
36 co-precipitation method.  
37  
38  
39  
40  
41  
42  
43

#### 44 **Acknowledgments**

45  
46  
47 Financial support from the National Natural Science Foundation of China (Grant No.  
48  
49 51764052) and Innovative Research Team (in Science and Technology) in University of  
50  
51 Yunnan Province.  
52  
53  
54  
55  
56  
57  
58  
59  
60  
61  
62  
63  
64  
65

## References

- [1] E. Roitero, F. Lasserre, M. Anglada, F. Mücklich, E. JiménezPiqué, A parametric study of laser interference surface patterning of dental zirconia: Effects of laser parameters on topography and surface quality, *Dent. Mater.* 33 (1) (2017) e28-e38.  
<https://doi.org/10.1016/j.dental.2016.09.040>.
- [2] S.M. Yong, D.H. Choi, K. Lee, S.Y. Ko, D.I. Cheong, Y.J. Park, S.I. Go, Study on carbon contamination and carboxylate group formation in  $Y_2O_3$ -MgO nanocomposites fabricated by spark plasma sintering, *J. Eur. Ceram. Soc.* 40 (3) (2019) 847-851.  
<https://doi.org/10.1016/j.jeurceramsoc.2019.10.035>.
- [3] J. Wang, L. Zhang, D. Chen, E.H. Jordan, M. Gell,  $Y_2O_3$ -MgO-ZrO<sub>2</sub> infrared transparent ceramic nanocomposites, *J. Am. Ceram. Soc.* 95 (3) (2012) 1033-1037.  
<https://doi.org/10.1111/j.1551-2916.2011.04928.x>.
- [4] J. Wen, T. Zhu, Z. Xie, W. Cao, W. Liu, A strategy to obtain a high-density and high-strength zirconia ceramic via ceramic injection molding by the modification of oleic acid, *Int. J. Min. Met. Mater.* 24 (6) (2017) 718-725. <https://doi.org/10.1007/s12613-017-1455-9>.
- [5] E. Jiménez-Piqué, A. Ramos, J.A. Muñoz-Tabares, A. Hatton, F. Soldera, F. Mücklich, M. Anglada, Focused ion beam tomography of zirconia degraded under hydrothermal conditions, *J. Eur. Ceram. Soc.* 32 (10) (2012) 2129-2136. <https://doi.org/10.1016/j.jeurceramsoc.2012.02.011>.
- [6] N. Wu, X.D. Li, J.G. Li, Q. Zhu, X.D. Sun, Fabrication of  $Gd_2O_3$  - MgO nanocomposite optical ceramics with varied crystallographic modifications of  $Gd_2O_3$  constituent, *J. Am. Ceram. Soc.* 101 (11) (2018) 4887-4891. <https://doi.org/10.1111/jace.15884>.
- [7] L.H. Liu, K.J. Morita, T.S. Suzuki, B.N. Kim, Synthesis of highly-infrared transparent  $Y_2O_3$ -MgO nanocomposites by colloidal technique and SPS, *Ceram. Int.* 46 (9) (2020) 13669-13676.  
<https://doi.org/10.1016/j.ceramint.2020.02.153>.
- [8] N. Safronova, O. Kryzhanovska, M. Dobrotvorska, A. Balabanov, A. Tolmachev, R. Yavetskiy, S. Parkhomenko, R.Y. Brodskii, V. Baumer, D.Y. Kosyanov, Influence of sintering temperature on structural and optical properties of  $Y_2O_3$ -MgO composite SPS ceramics, *Ceram. Int.* 46 (5) (2020) 6537-6543.  
<https://doi.org/10.1016/j.ceramint.2019.11.137>.

- 1  
2  
3  
4  
5  
6  
7  
8  
9  
10  
11  
12  
13  
14  
15  
16  
17  
18  
19  
20  
21  
22  
23  
24  
25  
26  
27  
28  
29  
30  
31  
32  
33  
34  
35  
36  
37  
38  
39  
40  
41  
42  
43  
44  
45  
46  
47  
48  
49  
50  
51  
52  
53  
54  
55  
56  
57  
58  
59  
60  
61  
62  
63  
64  
65
- [9] G. Urruth, D. Maury, C. Voisin, V. Baylac, D. Grossin, Powder bed selective laser processing (sintering/melting) of Yttrium Stabilized Zirconia using carbon-based material (TiC) as absorbance enhancer, *J. Eur. Ceram. Soc.* 42 (5) (2022) 2381-2390.  
<https://doi.org/10.1016/j.jeurceramsoc.2021.12.042>.
- [10] Z. Zeng, Y. Liu, Y. Zhang, Z. Zhou, X. Liu, Ferroelastic domain switching toughening in Ce-Y-La co-stabilized zirconia ceramics obtained from coated starting powders, *J. Alloy. Compd.* 820 (2020) 153177.  
<https://doi.org/10.1016/j.jallcom.2019.153177>.
- [11] J.H. Cheng, C.G. Tian, J. Yang, J.B. He, Electrical and mechanical properties of Sm<sub>2</sub>O<sub>3</sub> doped Y-TZP electrolyte ceramics, *Ceram. Int.* 44 (14) (2018) 17033-17037.  
<https://doi.org/10.1016/j.ceramint.2018.06.146>.
- [12] H. Nahor, Y. Kauffmann, W.D. Kaplan, The Cr-Doped Ni-YSZ (111) interface: Segregation, oxidation and the Ni equilibrium crystal shape, *Acta. Mater.* 166 (2019) 28-36.  
<https://doi.org/10.1016/j.actamat.2018.12.023>.
- [13] Y. Ling, X. Hao, Y. Gui, H. Qiu, Q. Li, H. Zheng, M. Omran, L. Gao, J. Chen, G. Chen, Stability properties and microstructure properties of microwave-sintered CeO<sub>2</sub> doped zirconia ceramics, *Ceram. Int.* 47 (20) (2021) 28210-28217. <https://doi.org/10.1016/j.ceramint.2021.06.234>.
- [14] N. Li, D. An, Z.Z. Yi, N.T. Yu, Z.P. Xie, Synthesis of 1Y6Ce-ZrO<sub>2</sub> nanoparticles with excellent sintering performance via novel Sol-Gel-Flux method, *Ceram. Int.* 48 (2) (2021) 2637-2644.  
<https://doi.org/10.1016/j.ceramint.2021.10.047>.
- [15] D.S. Kim, W.C. Kim, J.K. Lee, Effect of solid loading on the sintered properties of 3 mol% yttria-stabilized tetragonal zirconia polycrystals (3Y-TZP) ceramics via slip casting, *J. Nanosci. Nanotechno.* 19 (10) (2019) 6383-6386. <https://doi.org/10.1166/jnn.2019.17045>.
- [16] Y.Q. Ling, Q.N. Li, H.W. Zheng, M. Omran, L. Gao, J. Chen, G. Chen, Optimisation on the stability of CaO-doped partially stabilised zirconia by microwave heating, *Ceram. Int.* 47 (6) (2021) 8067-8074.  
<https://doi.org/10.1016/j.ceramint.2020.11.161>.
- [17] T.P. Wen, L. Yuan, T. Liu, Q.Y. Sun, E.D. Jin, C. Tian, J.K. Yu, Enhanced ionic conductivity and thermal shock resistance of MgO stabilized ZrO<sub>2</sub> doped with Y<sub>2</sub>O<sub>3</sub>, *Ceram. Int.* 46 (12) (2020) 19835-19842. <https://doi.org/10.1016/j.ceramint.2020.05.038>.

- 1  
2 [18] H.Y. Abed, M. Almasi-Kashi, S.A. Zaidan, Effect grain size on physical properties of  
3 (Y<sub>2</sub>O<sub>3</sub>-ZrO<sub>2</sub>-MgO-Al<sub>2</sub>O<sub>3</sub>) system, J. Phys.: Conf. Ser. 1178 (1) (2019) 012004.  
4 <https://doi.org/10.1088/1742-6596/1178/1/012004>.  
5
- 6 [19] J.L. Vazquez-Arce, H. Tiznado, R. Kirchheim, Onset of electronic conductivity in nanometer thick  
7 films of yttria stabilized zirconia (YSZ) at high electric fields, Acta Mater. 229 (2022) 117826.  
8 <https://doi.org/10.1016/j.actamat.2022.117826>.  
9
- 10 [20] N. Li, N.T. Yu, Z.Z. Yi, D. An, Z.P. Xie. CeO<sub>2</sub>-stabilised ZrO<sub>2</sub> nanoparticles with excellent sintering  
11 performances synthesized by sol-gel-flux method, J. Eur. Ceram. Soc. (2021).  
12 <https://doi.org/10.1016/j.jeurceramsoc.2021.12.012>.  
13
- 14 [21] M. Rad, S. Borhani, M. Moradi, V. Safarifard, Tuning the crystallinity of ZrO<sub>2</sub> nanostructures derived  
15 from thermolysis of Zr-based aspartic acid/succinic acid MOFs for energy storage application, Physica E.  
16 134 (2021) 114921. <https://doi.org/10.1016/j.physe.2021.114921>.  
17
- 18 [22] Z. Dong, Z. Ma, L. Yu, Y. Liu, Achieving high strength and ductility in ODS-W alloy by employing  
19 oxide@ W core-shell nanopowder as precursor, Nat. Commun. 12 (1) (2021) 1-10.  
20 <https://doi.org/10.1038/s41467-021-25283-2>.  
21
- 22 [23] P.T. Chung, S.H. Chiou, C.Y. Tseng, A.S.T. Chiang, Preparation and evaluation of a  
23 zirconia/oligosiloxane nanocomposite for LED encapsulation, ACS. Appl. Mater. Inter. 8(15) (2016)  
24 9986-9993. <https://doi.org/10.1021/acsami.6b02082>.  
25
- 26 [24] Y. Wei, Z. Zhao, J. Jiao, J. Liu, A. Duan, G. Jiang, Preparation of ultrafine Ce-based oxide  
27 nanoparticles and their catalytic performances for diesel soot combustion, J. Rare Earth. 32 (2) (2014)  
28 124-130. [https://doi.org/10.1016/s1002-0721\(14\)60041-7](https://doi.org/10.1016/s1002-0721(14)60041-7).  
29
- 30 [25] X. He, Z. Wang, D. Wang, F. Yang, R. Tang, J. Wang, Y. Pu, J. Chen, Sub-kilogram-scale synthesis of  
31 highly dispersible zirconia nanoparticles for hybrid optical resins, Appl. Surf. Sci. 491 (2019) 505-516.  
32 <https://doi.org/10.1016/j.apsusc.2019.06.187>.  
33
- 34 [26] K. Kosai, J. Yan, Effects of cyclic loading on subsurface microstructural changes of zirconia  
35 polycrystals in nanoscale mechanical processing, Int. J. Mach. Tool. Manu. 159 (2020) 103626.  
36 <https://doi.org/10.1016/j.ijmachtools.2020.103626>.  
37  
38  
39  
40  
41  
42  
43  
44  
45  
46  
47  
48  
49  
50  
51  
52  
53  
54  
55  
56  
57  
58  
59  
60  
61  
62  
63  
64  
65

- 1  
2 [27] L. Liu, S. Wang, B. Zhang, G. Jiang, J. Yang, Y. Li, W. Liu, J. Wang, W. Kong, From modification to  
3 mechanism: Supercritical hydrothermal synthesis of nano-zirconia, *Ceram. Int.* 48 (4) (2022) 4401-4423.  
4 <https://doi.org/10.1016/j.ceramint.2021.11.028>.  
5  
6  
7 [28] Y. Chang, S. Dong, H. Wang, K. Du, Q. Zhu, P. Luo, Synthesis of monodisperse spherical nanometer  
8  
9  
10  $ZrO_2$  ( $Y_2O_3$ ) powders via the coupling route of w/o emulsion with urea homogenous precipitation, *Mater.*  
11  
12 *Res. Bull.* 47 (3) (2012) 527-531. <https://doi.org/10.1016/j.materresbull.2011.12.055>.  
13  
14  
15 [29] S.M. Dezfuli, A. Shanaghi, S. Baghshahi, Effect of  $Al_2O_3$  and  $Y_2O_3$  on the corrosion behavior of  
16  
17  
18  $ZrO_2$ -benzotriazole nanostructured coatings applied on AA2024 via a sol-gel method, *Int. J. Min. Met.*  
19  
20  
21 *Mater.* 25 (11) (2018) 1344-1353. <https://doi.org/10.1007/s12613-018-1688-2>.  
22  
23 [30] S.J. Hao, C. Wang, T.L. Liu, Z.M. Mao, Z.Q. Mao, J.L. Wang, Fabrication of nanoscale yttria  
24  
25 stabilized zirconia for solid oxide fuel cell, *Int. J. Hydrogen Energ.* 42 (50) (2017) 29949-29959.  
26  
27 <https://doi.org/10.1016/j.ijhydene.2017.08.143>.  
28  
29 [31] J.J. Xia, H.R. Guo, M.Z. Cheng, C.Y. Chen, M.K. Wang, Y. Xiang, T.S. Li, E. Traversa, Electrospun  
30  
31 zirconia nanofibers for enhancing the electrochemical synthesis of ammonia by artificial nitrogen fixation,  
32  
33  
34 *J. Mater. Chem. A* 9 (4) (2021) 2145-2151.  
35  
36 <https://doi.org/10.1039/D0TA08089F>.  
37  
38 [32] K. VanEvery, M.J.M. Krane, R.W. Trice, Parametric study of suspension plasma spray processing  
39  
40 parameters on coating microstructures manufactured from nanoscale yttria-stabilized zirconia, *Surf. Coat.*  
41  
42 *Tech.* 206 (8-9) (2012) 2464-2473.  
43  
44 <https://doi.org/10.1016/j.surfcoat.2011.10.051>.  
45  
46 [33] B. Tyagi, K. Sidhpuria, B. Shaik, R.V. Jasra, Synthesis of nanocrystalline zirconia using sol-gel and  
47  
48 precipitation techniques, *Ind. Eng. Chem. Res.* 45 (25) (2006) 8643-8650.  
49  
50 <https://doi.org/10.1021/ie060519p>.  
51  
52 [34] M. Meepho, D. Wattasiriwech, S. Wattanasiriwech, P. Angwattana, Influence of reaction medium on  
53  
54 formation of nanocrystalline YSZ prepared by conventional and modified solvothermal process, *Energy*  
55  
56 *Procedia* 9 (1) (2011) 545-552. <https://doi.org/10.1016/j.egypro.2011.09.063>.  
57  
58  
59  
60  
61  
62  
63  
64  
65

- 1 [35] G. Roncallo, G. Cacciamani, E. Vacchieri, M. Ilatovskaia, I. Saenko, O. Fabrichnaya, Thermodynamic  
2 modeling and experimental investigation of the MgO - Y<sub>2</sub>O<sub>3</sub> - ZrO<sub>2</sub> system, *J. Am. Ceram. Soc.* 103 (9)  
3  
4  
5  
6 (2020) 5337-5353. <https://doi.org/10.1111/jace.17224>.
- 7 [36] J. Santoyo-Salazar, G. Gonzalez, J.A. Ascencio, J. Tartaj-Salvador, J.A. Chávez-Carvayar, Novel  
8 yttria-stabilised zirconia-alumina tetragonal phase obtained by co-precipitation, *J. Cryst. Growth* 290 (1)  
9  
10  
11 (2006) 307-312. <https://doi.org/10.1016/j.jcrysgro.2006.01.032>.
- 12 [37] Y.W. Hsu, K.H. Yang, K.M. Chang, S.W. Yeh, M.C. Wang, Synthesis and crystallisation behavior of 3  
13 mol% yttria stabilized tetragonal zirconia polycrystals (3Y-TZP) nanosized powders prepared using a  
14 simple co-precipitation process, *J. Alloy. Compd.* 509 (24) (2011) 6864-6870.  
15  
16  
17  
18  
19  
20  
21 <https://doi.org/10.1016/j.jallcom.2011.03.162>.
- 22 [38] X. He, Z. Wang, Y. Pu, D. Wang, R. Tang, S. Cui, J. Wang, J. Chen, High-gravity-assisted scalable  
23 synthesis of zirconia nanodispersion for light emitting diodes encapsulation with enhanced light extraction  
24 efficiency, *Chem. Eng. Sci.* 195 (2019) 1-10. <https://doi.org/10.1016/j.ces.2018.11.036>.
- 25 [39] Q. Feng, X. Ma, Q. Yan, C. Ge, Preparation of soft-agglomerated nano-sized ceramic powders by  
26 sol-gel combustion process, *Mat. Sci. Eng. B-ADV* 2009, 162(1): 53-58.  
27  
28  
29  
30  
31  
32  
33 <https://doi.org/10.1016/j.mseb.2009.02.007>.
- 34 [40] S. Salem, S. Jazayeri, F. Bondioli, A. Allahverdia, M. Shirvania, Characterizing thermal behavior of  
35 ceramic glaze containing nano-sized cobalt-aluminate pigment by hot stage microscopy, *Thermochim. acta*  
36 2011, 521(1-2): 191-196. <https://doi.org/10.1016/j.tca.2011.04.023>.
- 37 [41] H. Qiu, W. Huang, Y. Zhang, J. Chen, L. Gao, M. Omran, L. Nan, G. Chen, Preparation of nano-sized  
38 6MgO-2Y<sub>2</sub>O<sub>3</sub>-ZrO<sub>2</sub> powders by a combined co-precipitation and high energy ball milling process, *Ceram.*  
39  
40  
41  
42  
43  
44  
45  
46  
47  
48  
49  
50  
51  
52  
53  
54  
55  
56  
57  
58  
59  
60  
61  
62  
63  
64  
65  
66  
67  
68  
69  
70  
71  
72  
73  
74  
75  
76  
77  
78  
79  
80  
81  
82  
83  
84  
85  
86  
87  
88  
89  
90  
91  
92  
93  
94  
95  
96  
97  
98  
99  
100  
101  
102  
103  
104  
105  
106  
107  
108  
109  
110  
111  
112  
113  
114  
115  
116  
117  
118  
119  
120  
121  
122  
123  
124  
125  
126  
127  
128  
129  
130  
131  
132  
133  
134  
135  
136  
137  
138  
139  
140  
141  
142  
143  
144  
145  
146  
147  
148  
149  
150  
151  
152  
153  
154  
155  
156  
157  
158  
159  
160  
161  
162  
163  
164  
165  
166  
167  
168  
169  
170  
171  
172  
173  
174  
175  
176  
177  
178  
179  
180  
181  
182  
183  
184  
185  
186  
187  
188  
189  
190  
191  
192  
193  
194  
195  
196  
197  
198  
199  
200  
201  
202  
203  
204  
205  
206  
207  
208  
209  
210  
211  
212  
213  
214  
215  
216  
217  
218  
219  
220  
221  
222  
223  
224  
225  
226  
227  
228  
229  
230  
231  
232  
233  
234  
235  
236  
237  
238  
239  
240  
241  
242  
243  
244  
245  
246  
247  
248  
249  
250  
251  
252  
253  
254  
255  
256  
257  
258  
259  
260  
261  
262  
263  
264  
265  
266  
267  
268  
269  
270  
271  
272  
273  
274  
275  
276  
277  
278  
279  
280  
281  
282  
283  
284  
285  
286  
287  
288  
289  
290  
291  
292  
293  
294  
295  
296  
297  
298  
299  
300  
301  
302  
303  
304  
305  
306  
307  
308  
309  
310  
311  
312  
313  
314  
315  
316  
317  
318  
319  
320  
321  
322  
323  
324  
325  
326  
327  
328  
329  
330  
331  
332  
333  
334  
335  
336  
337  
338  
339  
340  
341  
342  
343  
344  
345  
346  
347  
348  
349  
350  
351  
352  
353  
354  
355  
356  
357  
358  
359  
360  
361  
362  
363  
364  
365  
366  
367  
368  
369  
370  
371  
372  
373  
374  
375  
376  
377  
378  
379  
380  
381  
382  
383  
384  
385  
386  
387  
388  
389  
390  
391  
392  
393  
394  
395  
396  
397  
398  
399  
400  
401  
402  
403  
404  
405  
406  
407  
408  
409  
410  
411  
412  
413  
414  
415  
416  
417  
418  
419  
420  
421  
422  
423  
424  
425  
426  
427  
428  
429  
430  
431  
432  
433  
434  
435  
436  
437  
438  
439  
440  
441  
442  
443  
444  
445  
446  
447  
448  
449  
450  
451  
452  
453  
454  
455  
456  
457  
458  
459  
460  
461  
462  
463  
464  
465  
466  
467  
468  
469  
470  
471  
472  
473  
474  
475  
476  
477  
478  
479  
480  
481  
482  
483  
484  
485  
486  
487  
488  
489  
490  
491  
492  
493  
494  
495  
496  
497  
498  
499  
500  
501  
502  
503  
504  
505  
506  
507  
508  
509  
510  
511  
512  
513  
514  
515  
516  
517  
518  
519  
520  
521  
522  
523  
524  
525  
526  
527  
528  
529  
530  
531  
532  
533  
534  
535  
536  
537  
538  
539  
540  
541  
542  
543  
544  
545  
546  
547  
548  
549  
550  
551  
552  
553  
554  
555  
556  
557  
558  
559  
560  
561  
562  
563  
564  
565  
566  
567  
568  
569  
570  
571  
572  
573  
574  
575  
576  
577  
578  
579  
580  
581  
582  
583  
584  
585  
586  
587  
588  
589  
590  
591  
592  
593  
594  
595  
596  
597  
598  
599  
600  
601  
602  
603  
604  
605  
606  
607  
608  
609  
610  
611  
612  
613  
614  
615  
616  
617  
618  
619  
620  
621  
622  
623  
624  
625  
626  
627  
628  
629  
630  
631  
632  
633  
634  
635  
636  
637  
638  
639  
640  
641  
642  
643  
644  
645  
646  
647  
648  
649  
650  
651  
652  
653  
654  
655  
656  
657  
658  
659  
660  
661  
662  
663  
664  
665  
666  
667  
668  
669  
670  
671  
672  
673  
674  
675  
676  
677  
678  
679  
680  
681  
682  
683  
684  
685  
686  
687  
688  
689  
690  
691  
692  
693  
694  
695  
696  
697  
698  
699  
700  
701  
702  
703  
704  
705  
706  
707  
708  
709  
710  
711  
712  
713  
714  
715  
716  
717  
718  
719  
720  
721  
722  
723  
724  
725  
726  
727  
728  
729  
730  
731  
732  
733  
734  
735  
736  
737  
738  
739  
740  
741  
742  
743  
744  
745  
746  
747  
748  
749  
750  
751  
752  
753  
754  
755  
756  
757  
758  
759  
760  
761  
762  
763  
764  
765  
766  
767  
768  
769  
770  
771  
772  
773  
774  
775  
776  
777  
778  
779  
780  
781  
782  
783  
784  
785  
786  
787  
788  
789  
790  
791  
792  
793  
794  
795  
796  
797  
798  
799  
800  
801  
802  
803  
804  
805  
806  
807  
808  
809  
810  
811  
812  
813  
814  
815  
816  
817  
818  
819  
820  
821  
822  
823  
824  
825  
826  
827  
828  
829  
830  
831  
832  
833  
834  
835  
836  
837  
838  
839  
840  
841  
842  
843  
844  
845  
846  
847  
848  
849  
850  
851  
852  
853  
854  
855  
856  
857  
858  
859  
860  
861  
862  
863  
864  
865  
866  
867  
868  
869  
870  
871  
872  
873  
874  
875  
876  
877  
878  
879  
880  
881  
882  
883  
884  
885  
886  
887  
888  
889  
890  
891  
892  
893  
894  
895  
896  
897  
898  
899  
900  
901  
902  
903  
904  
905  
906  
907  
908  
909  
910  
911  
912  
913  
914  
915  
916  
917  
918  
919  
920  
921  
922  
923  
924  
925  
926  
927  
928  
929  
930  
931  
932  
933  
934  
935  
936  
937  
938  
939  
940  
941  
942  
943  
944  
945  
946  
947  
948  
949  
950  
951  
952  
953  
954  
955  
956  
957  
958  
959  
960  
961  
962  
963  
964  
965  
966  
967  
968  
969  
970  
971  
972  
973  
974  
975  
976  
977  
978  
979  
980  
981  
982  
983  
984  
985  
986  
987  
988  
989  
990  
991  
992  
993  
994  
995  
996  
997  
998  
999  
1000

Table 1. Experimental drug specifications and manufacturer.

Name	Standards	Manufacturer
ZrOCl <sub>2</sub> ·8H <sub>2</sub> O	AR, ≥ 99.0%	Sinopharm Chemical Reagent Co. , LTD
MgCl <sub>2</sub> ·6H <sub>2</sub> O	AR, ≥ 98.0%	Sinopharm Chemical Reagent Co. , LTD
Y(NO <sub>3</sub> ) <sub>3</sub> ·6H <sub>2</sub> O	AR, ≥ 99.99%	Shanghai Aladdin Biochemical Technology Co. , LTD
NH <sub>3</sub> ·H <sub>2</sub> O	AR, 25–28%	Jiangsu Qiangsheng Functional Chemistry Co. , LTD
AgNO <sub>3</sub>	AR, 0.1000mol/L	Yida Technology Co. , LTD
CH <sub>3</sub> CH <sub>2</sub> OH	AR	Tianjin Zhiyuan Chemical Reagent Co. , LTD
UP H <sub>2</sub> O	18MΩ.cm	Laboratory homebrew

Table 2. Experimental instruments and equipment.

Name	Model
X-ray Diffraction	Bruker D8 Advance A25×
Renishaw Raman Microscope System	inVia
Field Emission Scanning Electron Microscopy	NOVA NANOSEM-450
Fourier Transform Infrared Spectroscopy	NICOLET-IS10, Nicolet, USA
Thermal Gravimetric Analyzer	NETZSCH STAA49F31
Brunner Emmet Teller	BELSORP-max II
Transmission Electron Microscopy	JEM-2100
Planetary Ball Mill	QM-3SP4

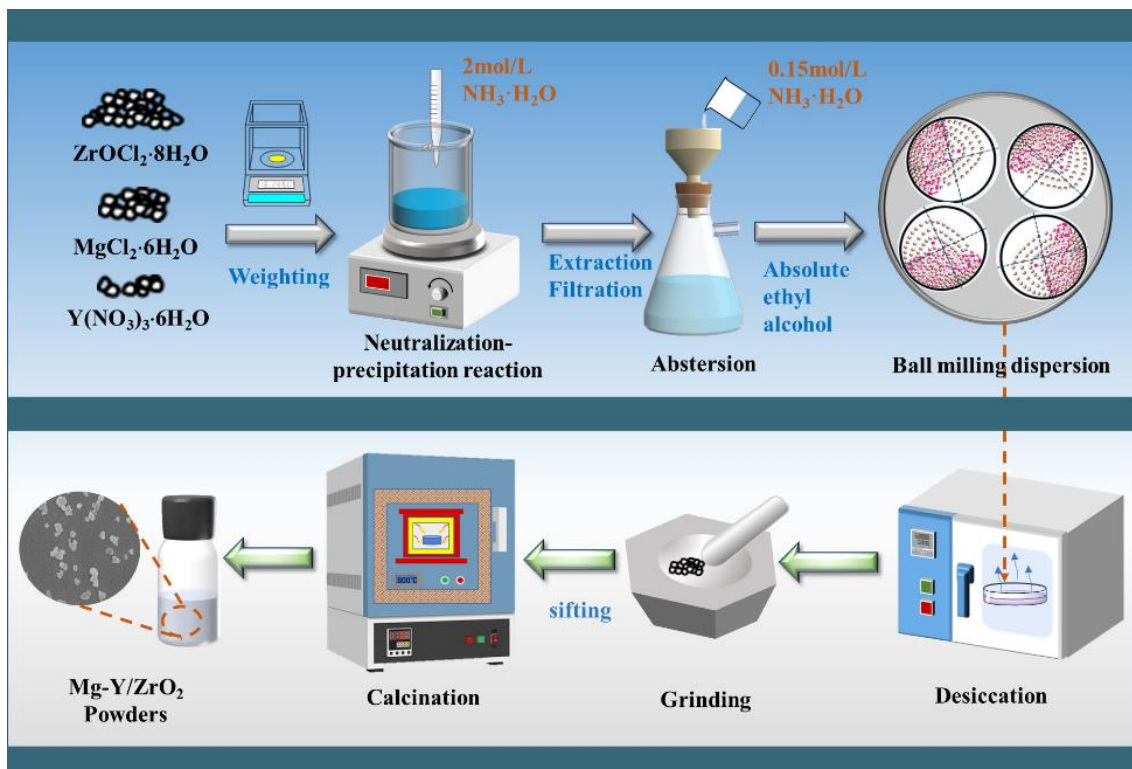


Fig. 1 Experimental flow diagram of the preparation of nanoscale *t*-Mg-Y/ZrO<sub>2</sub> samples using co-precipitation method.

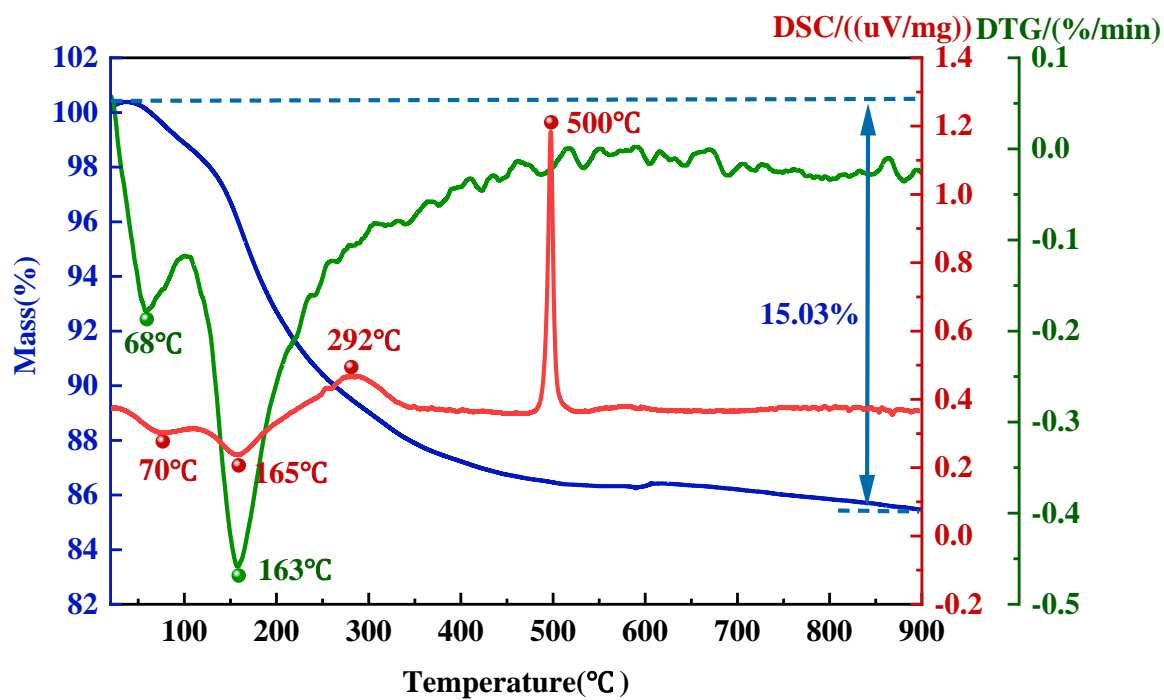


Fig. 2 TG-DSC curves of the precursor samples prepared by ball milling for 6 h.

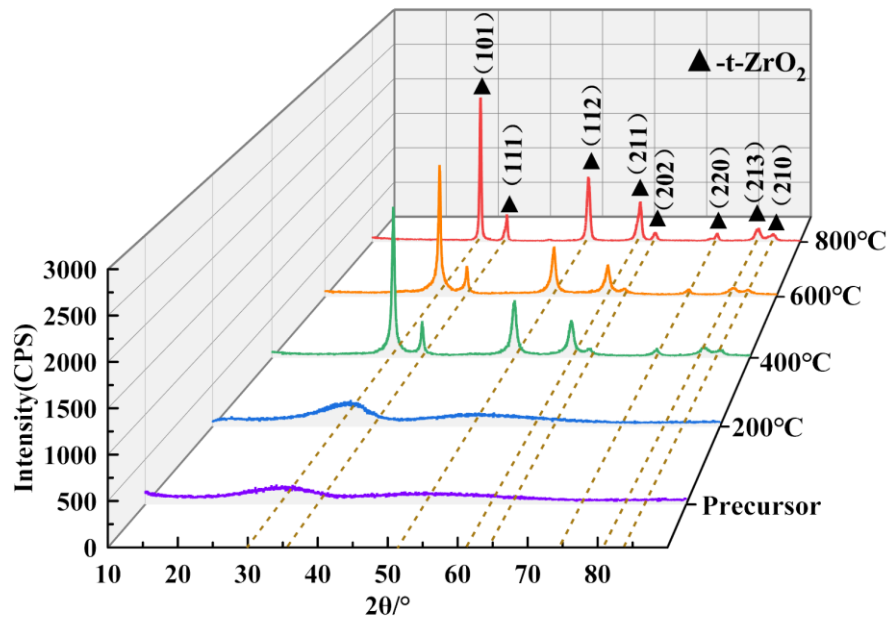


Fig. 3 XRD spectra of zirconia powders prepared under experimental conditions of precursors and calcination temperatures of 200–800 °C.

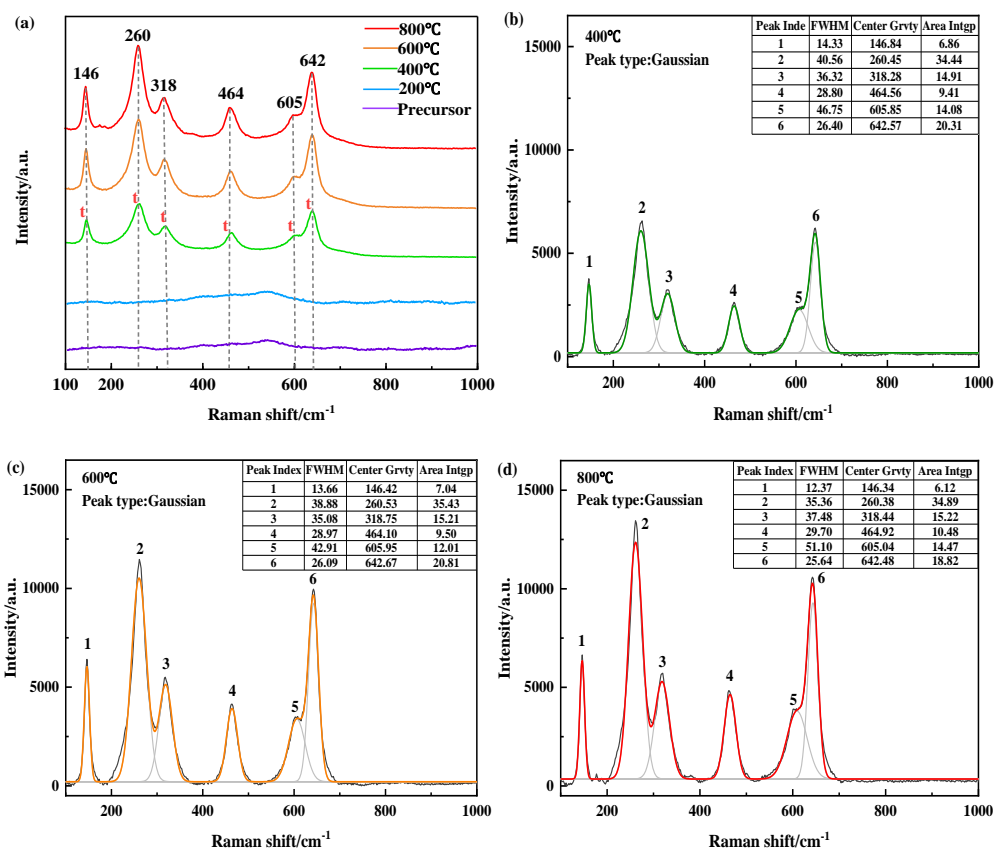


Fig. 4 (a) Raman spectra at different calcination temperatures. (b), (c), and (d) Gaussian fitted Raman curves at calcination temperatures of 400–800 °C.

1  
2  
3  
4  
5  
6  
7  
8  
9  
10  
11  
12  
13  
14  
15  
16  
17  
18  
19  
20  
21  
22  
23  
24  
25  
26  
27  
28  
29  
30  
31  
32  
33  
34  
35  
36  
37  
38  
39  
40  
41  
42  
43  
44  
45  
46  
47  
48  
49  
50  
51  
52  
53  
54  
55  
56  
57  
58  
59  
60  
61  
62  
63  
64  
65

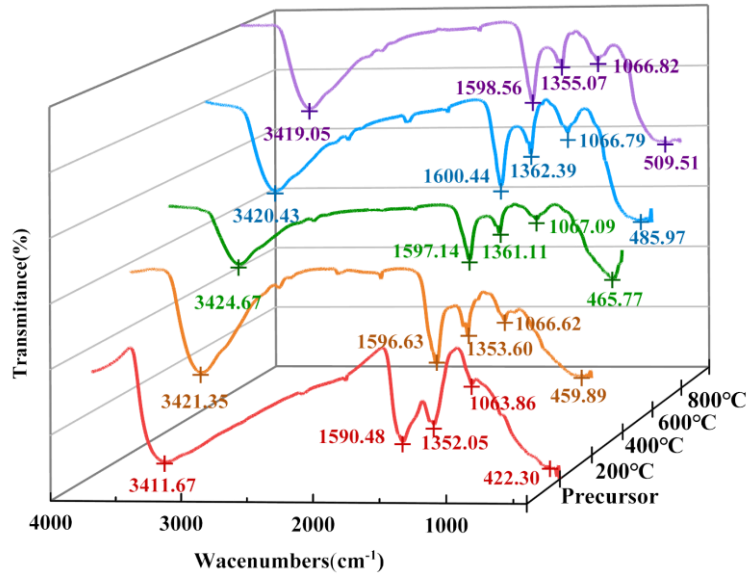


Fig. 5 FTIR spectra of precursors and zirconia nanopowders prepared at different calcination temperatures.

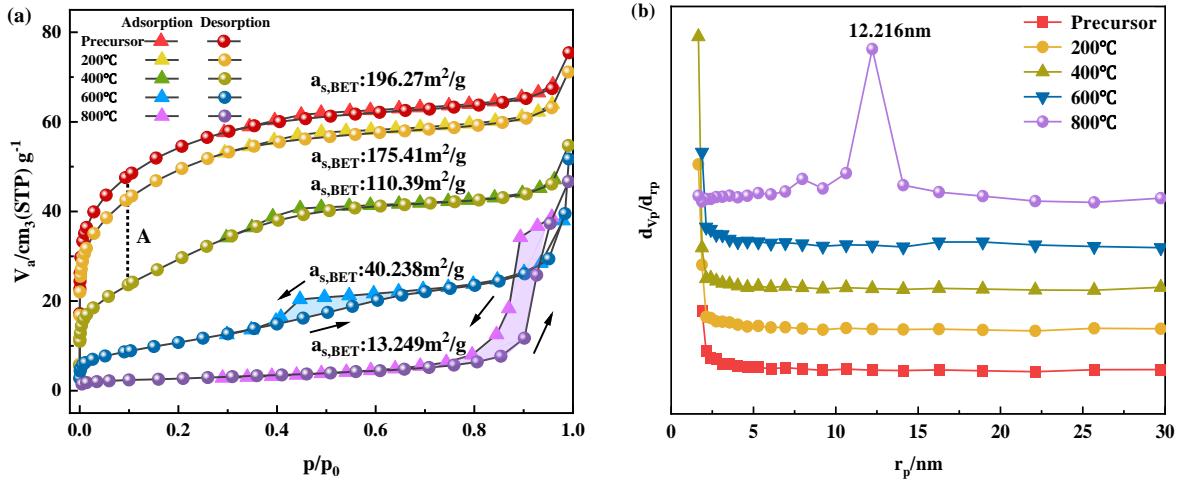


Fig. 6 Nitrogen adsorption-desorption curves and PSD curves of precursors and zirconia nanopowders prepared at calcination temperatures of 200–800 °C.

1  
2  
3  
4  
5  
6  
7  
8  
9  
10  
11  
12  
13  
14  
15  
16  
17  
18  
19  
20  
21  
22  
23  
24  
25  
26  
27  
28  
29  
30  
31  
32  
33  
34  
35  
36  
37  
38  
39  
40  
41  
42  
43  
44  
45  
46  
47  
48  
49  
50  
51  
52  
53  
54  
55  
56  
57  
58  
59  
60  
61  
62  
63  
64  
65

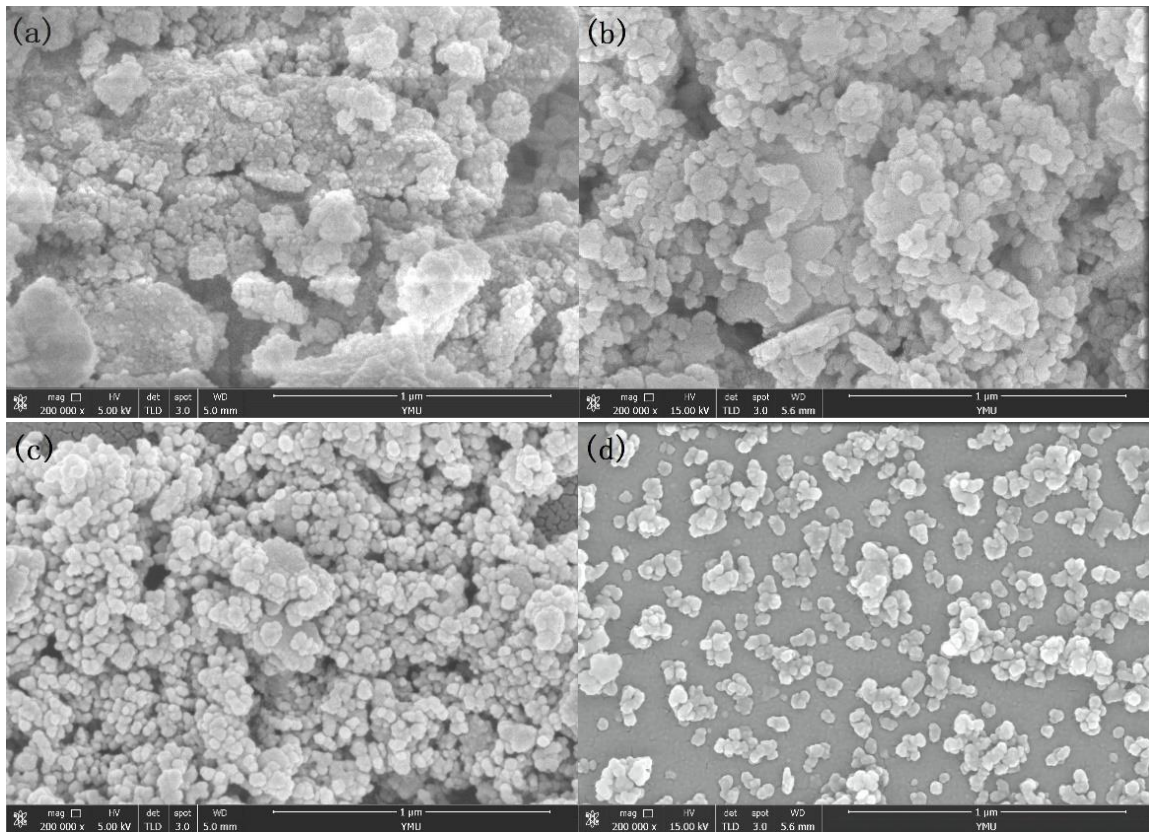


Fig. 7 (a)–(d) shows the SEM images of zirconia nanopowders obtained at different calcination temperatures of 200–800 °C.

1 **Co-precipitation of nano Mg-Y/ZrO<sub>2</sub> ternary oxide eutectic system: Effects of**  
2  
3  
4 **calcination temperature**  
5  
6  
7

8  
9 Hongju Qiu <sup>a</sup>, Weiwei Huang <sup>a</sup>, Yanqiong Zhang <sup>a</sup>, Jin Chen <sup>a, \*\*</sup>, Lei Gao <sup>a, \*\*</sup>,  
10  
11 Mamdouh Omran <sup>b</sup>, Li Nan<sup>c</sup>, Guo Chen <sup>a, \*</sup>  
12  
13  
14  
15  
16

17 <sup>a</sup> Kunming Key Laboratory of Energy Materials Chemistry, Yunnan Minzu University,  
18  
19 Kunming 650500, Yunnan, P.R. China.  
20  
21

22 <sup>b</sup> Process Metallurgy Research Group, Faculty of Technology, University of Oulu, Finland.  
23  
24

25 <sup>c</sup> College of Chemistry and Resources Engineering, Hong He University, Mengzi, China,  
26  
27 661199  
28  
29  
30

31  
32  
33 \* Corresponding author: guochen@kust.edu.cn  
34  
35

36 \* Corresponding author: glkust2013@hotmail.com, jinchen@kust.edu.cn  
37  
38  
39  
40  
41

42 **Abstract:** In the family of inorganic nanomaterials, zirconia is a highly promising functional ceramic  
43  
44 with a high refractive index, hardness, and dielectric constant, as well as excellent chemical inertness and  
45  
46 thermal stability. These properties are enhanced in nano-zirconia ceramics, because nanopowders have a  
47  
48 small particle size, good morphology, and uniform and dispersive distribution. In this study, a  
49  
50 co-precipitation process was proposed to synthesise highly dispersed MgO-Y<sub>2</sub>O<sub>3</sub> co-stabilized ZrO<sub>2</sub>  
51  
52  
53 nanopowders. The effects of different calcination temperatures on the crystallisation degree and particle  
54  
55  
56 dispersion of zirconia nanopowders were characterised by X-ray diffraction (XRD),  
57  
58  
59  
60  
61  
62  
63  
64  
65

1 thermogravimetry-differential scanning calorimetry (TG-DSC), Raman spectroscopy, Fourier transform  
2  
3 infrared spectroscopy (FTIR), nitrogen adsorption using the Brunauer–Emmett–Teller (BET) theory,  
4  
5  
6 transmission electron microscopy (TEM), and field emission scanning electron microscopy (FESEM). The  
7  
8  
9 optimum synthesis conditions were obtained as follows: 6 h of high-energy planetary grinding and  
10  
11 calcination at 800 °C in an electric furnace. Under these optimum conditions, the average particle size of  
12  
13 the prepared powder was 28.7 nm. This process enriches the literature on the controllable preparation of  
14  
15  
16  
17 Mg-Y/ZrO<sub>2</sub> nanopowders obtained by the co-precipitation method.

18  
19  
20 **Keywords:** Mg-Y/ZrO<sub>2</sub>; Nanopowders; Co-precipitation; Crystallisation degree; Particle dispersion;  
21  
22  
23  
24

## 25 **1. Introduction**

26

27  
28 Zirconia is an important inorganic nonmetallic material with applications in ceramics, catalysts,  
29  
30 refractories, optics, aerospace, biology, and chemistry [1-4]. However, pure zirconia materials exhibit  
31  
32  
33  
34 volume change effects during the reversible martensitic transformation between the monoclinic phase and  
35  
36 tetragonal crystals, leading to a decline in their mechanical and thermal shock properties, which limits their  
37  
38  
39 application range [5-8].  
40

41  
42 To resolve this issue, studies have reported that the phase stability of pure zirconia materials may be  
43  
44 improved by co-doping zirconia with stabilisers, thus enhancing their mechanical properties and thermal  
45  
46 shock resistance [9-12]. Common stabilisers include oxides such as Y<sub>2</sub>O<sub>3</sub>, CaO, Al<sub>2</sub>O<sub>3</sub>, MgO, Sc<sub>2</sub>O, and  
47  
48  
49 CeO<sub>2</sub> [13-15]. The stable states of the zirconia materials generally include: tetragonal zirconia  
50  
51 polycrystalline (TZP), fully stabilized zirconia (FSZ), and partially stabilized zirconia (PSZ) [16]. Wen et al.  
52  
53 [17] investigated the improvement in the phase composition, packing density, microstructure, and  
54  
55  
56  
57  
58 compressive strength of MgO-PSZ ceramics by doping with a Y<sub>2</sub>O<sub>3</sub> stabiliser. The good performance of  
59  
60  
61  
62  
63  
64  
65

1 zirconia ceramics was reported to be owing to the ultrafine particle diameter and a reasonable proportion of  
2  
3 stabilisers. Abed et al. [18] explored the effect of the grain size of  $Y_2O_3$ - $ZrO_2$ - $MgAl_2O_4$  powders on the  
4  
5 properties of ceramic sintered bodies. The grain size greatly influenced the properties of zirconia ceramics,  
6  
7 in addition to the effect of stabiliser content. Therefore, the grain size and dispersion of the precursor  
8  
9 material are considered key factors in the preparation of high-toughness and high-strength zirconia  
10  
11 materials.  
12  
13  
14  
15  
16

17 Currently, the study of ultrafine nanoscale zirconia materials is attracting increasing attention [19,20].  
18  
19 Nanoparticles are solid particles with sizes in the range of 0.1–100 nm, between bulk materials and atoms  
20  
21 and molecules, and serve as the raw materials in nanotechnology [21]. Nanosystems have properties, such  
22  
23 as the small size, dielectric limit, and quantum tunnelling effects, which are not present in macroscopic  
24  
25 systems (with objects visible to the human eye as the lower limit) or mesoscopic systems (submicron level,  
26  
27 0.1–1  $\mu$ m). Therefore, nanosystems exhibit high catalytic activity and selectivity, high adsorption and  
28  
29 diffusion, and excellent optical properties (such as high transparency and magnetic properties), enhanced  
30  
31 toughness, lubricity, and other physical and chemical properties, which creates great potential for the  
32  
33 application of nanomaterials [22-24]. However, owing to the high surface energy of nanoparticles and van  
34  
35 der Waals forces between particles, nanoparticles are highly prone to agglomeration during preparation,  
36  
37 separation, storage, and application, which affects the advantages gained by the small size of these  
38  
39 materials. Therefore, maintaining good precursor dispersion and inhibiting nanoparticle agglomeration are  
40  
41 important research topics in nanotechnology [25,26].  
42  
43  
44  
45  
46  
47  
48  
49  
50  
51

52 Many methods are available for the preparation of nanoscale zirconia. Currently, wet chemical  
53  
54 preparation methods, such as hydrothermal [27], precipitation [28], sol-gel [29], microemulsion [30],  
55  
56 electrochemical synthesis [31], and solvent evaporation [32], are used. During chemical precipitation, a  
57  
58  
59  
60  
61  
62  
63  
64  
65

1 precipitant is added to a mixed solution to produce insoluble precipitates, such as hydroxides or sulfates.

2  
3 The precipitates serve as the raw precursors. After the subsequent washing-filtering-heating process,

4  
5  
6 precursors decompose into powder products. Chemical precipitation [33] is often selected for the

7  
8  
9 preparation of powder products at the laboratory scale because of its low reactant count and equipment

10  
11 requirements, ease of operation, and high product purity. To prepare nanopowders, including multiple

12  
13  
14 oxides, the chemical method of co-precipitation is widely used [34,35].

15  
16  
17 Co-precipitation has been successfully applied to the preparation of nanoscale zirconia. Santoyo et al.

18  
19  
20 [36] used this method to obtain nanoscale tetragonal-phase zirconia. Yttrium oxide (3 mol%) partially

21  
22 stabilised zirconia particles were dissolved in an  $\text{Al}(\text{NO}_3)_3 \cdot 9\text{H}_2\text{O}$  solution and subsequently co-precipitated

23  
24  
25 with ammonia to obtain 3 mol% YSZ- $\text{Al}_2\text{O}_3$  particles (the target precursor). The target precursor was

26  
27  
28 washed with ultrapure water and anhydrous ethanol, followed by drying in an oven at 90 °C. Subsequently,

29  
30 the precursor sample was calcined at 300 °C for 20 h to obtain  $\text{Al}_2\text{O}_3$  and  $\text{Y}_2\text{O}_3$  stabilized zirconium

31  
32  
33 dioxide nanopowders. The cold pressed nanopowders were sintered in air at 1100 °C for 6 h to obtain

34  
35  
36 YSZ- $\text{Al}_2\text{O}_3$  ceramics. Hsu et al. [37] obtained tetragonal-phase  $\text{ZrO}_2$  with a size of 21.3 nm using the

37  
38  
39 co-precipitation method.

40  
41  
42 In this study, a co-precipitation process is proposed to prepare highly dispersed yttrium oxide and

43  
44  
45 magnesium oxide-stabilised zirconium oxide nanopowders.  $\text{ZrOCl}_2 \cdot 8\text{H}_2\text{O}$  is used as the zirconium source

46  
47  
48 mixed with  $\text{Y}(\text{NO}_3)_3 \cdot 6\text{H}_2\text{O}$  and  $\text{MgCl}_2 \cdot 6\text{H}_2\text{O}$ . The mixture is co-precipitated by titration with  $\text{NH}_3 \cdot \text{H}_2\text{O}$

49  
50  
51 under high-speed stirring, and nanoscale zirconium oxide powder is produced after extraction and

52  
53  
54 subsequent washing, ball milling, drying, and calcination. The obtained samples are characterised by

55  
56  
57 thermogravimetry-differential scanning calorimetry (TG-DSC), X-ray diffraction (XRD), Raman

58  
59  
60 spectroscopy, Fourier transform infrared spectroscopy (FTIR), nitrogen adsorption using the Brunauer–

61  
62  
63  
64  
65

1 Emmett–Teller (BET) theory, transmission electron microscopy (TEM), and field emission scanning  
2  
3 electron microscopy (FESEM). The effects of the calcination temperature on the degree of crystallisation,  
4  
5 physical phase composition, and particle dispersion of the final tetragonal-phase Mg-Y/ZrO<sub>2</sub> (*t*-Mg-Y/ZrO<sub>2</sub>)  
6  
7  
8 are investigated.  
9

## 10 11 12 13 14 **2. Experiments**

### 15 16 17 **2.1 Materials**

18  
19 The chemicals used in the experimental process are listed in Table 1, and the apparatus and equipment  
20  
21 used are listed in Table 2.  
22  
23

### 24 25 **2.2 Preparation of Mg-Y/ZrO<sub>2</sub> nanoparticles**

26  
27 Firstly, 0.002 mol Y(NO<sub>3</sub>)<sub>3</sub>·6H<sub>2</sub>O, 0.006 mol MgCl<sub>2</sub>·6H<sub>2</sub>O, and 0.092 mol ZrOCl<sub>2</sub>·8H<sub>2</sub>O were  
28  
29 accurately weighed using an analytical balance and mixed to prepare a 0.1 mol/L sample solution.  
30  
31 Subsequently, 150 mL of a 25–28 % ammonia solution was diluted to prepare a 2 mol/L ammonia solution  
32  
33 using a measuring cylinder (sealed with cling film to prevent ammonia evaporation). For the precipitation  
34  
35 process, the 2 mol/L dilute ammonia solution was added dropwise to the sample solution under high-speed  
36  
37 magnetic stirring. The pH at the end of the titration was controlled to 10 to ensure complete precipitation of  
38  
39 Zr<sup>4+</sup>, Mg<sup>2+</sup> and Y<sup>3+</sup>. After aging, the sample was washed four times with 0.15 mol/L dilute ammonia  
40  
41 solution, and then washed once with anhydrous ethanol. The last washing solution was tested for the  
42  
43 absence of white Cl<sup>-</sup> precipitation using a 0.1000 mol/L AgNO<sub>3</sub> solution. The washed samples were then  
44  
45 dispersed in an anhydrous ethanol medium, subjected to high-energy planetary ball milling (for 6 h), and  
46  
47 subsequently dried. The dried powder was finely ground in a grinding pot and passed through an 80-mesh  
48  
49 sieve. Calcination was performed in a medium-ring electric furnace using specially designed temperatures  
50  
51  
52  
53  
54  
55  
56  
57  
58  
59  
60  
61  
62  
63  
64  
65

1 (200–800 °C). Subsequently, the calcined powder was passed through a 200-mesh sieve. The  
2  
3  
4  
5  
6  
7  
8  
9  
10  
11  
12  
13  
14  
15  
16  
17  
18  
19  
20  
21  
22  
23  
24  
25  
26  
27  
28  
29  
30  
31  
32  
33  
34  
35  
36  
37  
38  
39  
40  
41  
42  
43  
44  
45  
46  
47  
48  
49  
50  
51  
52  
53  
54  
55  
56  
57  
58  
59  
60  
61  
62  
63  
64  
65

(200–800 °C). Subsequently, the calcined powder was passed through a 200-mesh sieve. The  
aforementioned well-designed experimental procedure was used to investigate the optimum conditions for  
the preparation of highly dispersed, high-quality *t*-Mg-Y/ZrO<sub>2</sub> nanopowder materials (as shown in Fig. 1).

## 2.3 Characterisation of as-prepared Mg-Y/ZrO<sub>2</sub> nanoparticles

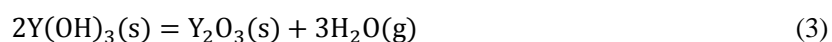
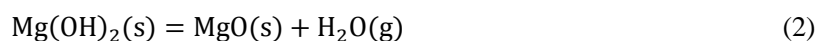
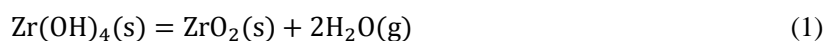
The crystalline phase composition of zirconia nanopowders is a key factor in characterising their  
properties. In this study, a thermal gravimetric analyser (TGA) was used to measure the change in material  
mass with temperature (and time) to observe the quantitative and qualitative variations in temperature  
during the generation of zirconia powders from their precursors, and thus analyse the thermal stability of  
the material. The powder samples were qualitatively characterised by XRD, and the crystallinity of these  
samples was analysed (scanning speed of 5 °/min). Furthermore, XRD results were analysed using Jade  
software and Scherrer's equation to calculate the zirconia grain size. The molecular vibration of the samples  
was characterised by Raman spectroscopy. The powder surface adsorption energy and pore size variation  
were characterized by nitrogen adsorption using the BET theory. A combination of FTIR with computer  
technology was used to characterise the chemical structure of the surface of the powder particles using  
interferograms, in a test spectrum range of 500–4000 cm<sup>-1</sup>. The FESEM instrument had a ultra-high  
resolution that was used to magnify zirconia nanopowders in a low-vacuum environment to monitor the  
microscopic morphology of the sample.

## 3. Results and discussion

### 3.1 TG-DSC characterisation

Characterisation by TG-DSC was used to obtain the weight loss of the sample during the heating  
process, and it was further used to characterise the changes in the precursor at different temperature stages.

1 The atmosphere used for TG-DSC analysis was air, the ramp rate was 5 °C/min, and the test temperature  
2  
3 range was 18–900 °C. Figure 2 shows the TG-DSC curve of the precursor samples, which initially  
4  
5 decreased rapidly and then gradually flattened. This was mainly owing to the loss of a large quantity of free  
6  
7 and bound water from the precursor, with a total burn loss of 15.03 %. The DSC curve shows two thermal  
8  
9 absorption peaks at 70 and 165 °C, combined with the TG and differential thermogravimetry (DTG) curves.  
10  
11 The thermal absorption peak at 70 °C was attributed to the loss of adsorbed and bound water, while the  
12  
13 thermal absorption peak at 165 °C was associated with the dehydrative decomposition of zirconium,  
14  
15 magnesium, and yttrium hydroxides during their transformations to ZrO<sub>2</sub>, MgO<sub>2</sub> and Y<sub>2</sub>O<sub>3</sub> as follows:  
16  
17  
18  
19  
20  
21



25  
26  
27  
28  
29  
30  
31 Additionally, two exothermic peaks were observed at 292 and 500 °C in the DSC curves. The peak at  
32  
33 292 °C was weak because the transformation of amorphous zirconia was in the initial stage. Furthermore,  
34  
35 the peak at 500 °C was extremely strong, but the corresponding weight loss in the TG and DTG curves was  
36  
37 absent. This result was because of the specific chemical reactions that caused the exothermic peaks by  
38  
39 generating large amounts of heat, which had an important effect on the crystallisation of zirconia  
40  
41  
42  
43  
44  
45  
46  
47  
48  
49  
50  
51  
52  
53  
54  
55  
56  
57  
58  
59  
60  
61  
62  
63  
64  
65  
66  
67  
68  
69  
70  
71  
72  
73  
74  
75  
76  
77  
78  
79  
80  
81  
82  
83  
84  
85  
86  
87  
88  
89  
90  
91  
92  
93  
94  
95  
96  
97  
98  
99  
100  
101  
102  
103  
104  
105  
106  
107  
108  
109  
110  
111  
112  
113  
114  
115  
116  
117  
118  
119  
120  
121  
122  
123  
124  
125  
126  
127  
128  
129  
130  
131  
132  
133  
134  
135  
136  
137  
138  
139  
140  
141  
142  
143  
144  
145  
146  
147  
148  
149  
150  
151  
152  
153  
154  
155  
156  
157  
158  
159  
160  
161  
162  
163  
164  
165  
166  
167  
168  
169  
170  
171  
172  
173  
174  
175  
176  
177  
178  
179  
180  
181  
182  
183  
184  
185  
186  
187  
188  
189  
190  
191  
192  
193  
194  
195  
196  
197  
198  
199  
200  
201  
202  
203  
204  
205  
206  
207  
208  
209  
210  
211  
212  
213  
214  
215  
216  
217  
218  
219  
220  
221  
222  
223  
224  
225  
226  
227  
228  
229  
230  
231  
232  
233  
234  
235  
236  
237  
238  
239  
240  
241  
242  
243  
244  
245  
246  
247  
248  
249  
250  
251  
252  
253  
254  
255  
256  
257  
258  
259  
260  
261  
262  
263  
264  
265  
266  
267  
268  
269  
270  
271  
272  
273  
274  
275  
276  
277  
278  
279  
280  
281  
282  
283  
284  
285  
286  
287  
288  
289  
290  
291  
292  
293  
294  
295  
296  
297  
298  
299  
300  
301  
302  
303  
304  
305  
306  
307  
308  
309  
310  
311  
312  
313  
314  
315  
316  
317  
318  
319  
320  
321  
322  
323  
324  
325  
326  
327  
328  
329  
330  
331  
332  
333  
334  
335  
336  
337  
338  
339  
340  
341  
342  
343  
344  
345  
346  
347  
348  
349  
350  
351  
352  
353  
354  
355  
356  
357  
358  
359  
360  
361  
362  
363  
364  
365  
366  
367  
368  
369  
370  
371  
372  
373  
374  
375  
376  
377  
378  
379  
380  
381  
382  
383  
384  
385  
386  
387  
388  
389  
390  
391  
392  
393  
394  
395  
396  
397  
398  
399  
400  
401  
402  
403  
404  
405  
406  
407  
408  
409  
410  
411  
412  
413  
414  
415  
416  
417  
418  
419  
420  
421  
422  
423  
424  
425  
426  
427  
428  
429  
430  
431  
432  
433  
434  
435  
436  
437  
438  
439  
440  
441  
442  
443  
444  
445  
446  
447  
448  
449  
450  
451  
452  
453  
454  
455  
456  
457  
458  
459  
460  
461  
462  
463  
464  
465  
466  
467  
468  
469  
470  
471  
472  
473  
474  
475  
476  
477  
478  
479  
480  
481  
482  
483  
484  
485  
486  
487  
488  
489  
490  
491  
492  
493  
494  
495  
496  
497  
498  
499  
500  
501  
502  
503  
504  
505  
506  
507  
508  
509  
510  
511  
512  
513  
514  
515  
516  
517  
518  
519  
520  
521  
522  
523  
524  
525  
526  
527  
528  
529  
530  
531  
532  
533  
534  
535  
536  
537  
538  
539  
540  
541  
542  
543  
544  
545  
546  
547  
548  
549  
550  
551  
552  
553  
554  
555  
556  
557  
558  
559  
560  
561  
562  
563  
564  
565  
566  
567  
568  
569  
570  
571  
572  
573  
574  
575  
576  
577  
578  
579  
580  
581  
582  
583  
584  
585  
586  
587  
588  
589  
590  
591  
592  
593  
594  
595  
596  
597  
598  
599  
600  
601  
602  
603  
604  
605  
606  
607  
608  
609  
610  
611  
612  
613  
614  
615  
616  
617  
618  
619  
620  
621  
622  
623  
624  
625  
626  
627  
628  
629  
630  
631  
632  
633  
634  
635  
636  
637  
638  
639  
640  
641  
642  
643  
644  
645  
646  
647  
648  
649  
650  
651  
652  
653  
654  
655  
656  
657  
658  
659  
660  
661  
662  
663  
664  
665  
666  
667  
668  
669  
670  
671  
672  
673  
674  
675  
676  
677  
678  
679  
680  
681  
682  
683  
684  
685  
686  
687  
688  
689  
690  
691  
692  
693  
694  
695  
696  
697  
698  
699  
700  
701  
702  
703  
704  
705  
706  
707  
708  
709  
710  
711  
712  
713  
714  
715  
716  
717  
718  
719  
720  
721  
722  
723  
724  
725  
726  
727  
728  
729  
730  
731  
732  
733  
734  
735  
736  
737  
738  
739  
740  
741  
742  
743  
744  
745  
746  
747  
748  
749  
750  
751  
752  
753  
754  
755  
756  
757  
758  
759  
760  
761  
762  
763  
764  
765  
766  
767  
768  
769  
770  
771  
772  
773  
774  
775  
776  
777  
778  
779  
780  
781  
782  
783  
784  
785  
786  
787  
788  
789  
790  
791  
792  
793  
794  
795  
796  
797  
798  
799  
800  
801  
802  
803  
804  
805  
806  
807  
808  
809  
810  
811  
812  
813  
814  
815  
816  
817  
818  
819  
820  
821  
822  
823  
824  
825  
826  
827  
828  
829  
830  
831  
832  
833  
834  
835  
836  
837  
838  
839  
840  
841  
842  
843  
844  
845  
846  
847  
848  
849  
850  
851  
852  
853  
854  
855  
856  
857  
858  
859  
860  
861  
862  
863  
864  
865  
866  
867  
868  
869  
870  
871  
872  
873  
874  
875  
876  
877  
878  
879  
880  
881  
882  
883  
884  
885  
886  
887  
888  
889  
890  
891  
892  
893  
894  
895  
896  
897  
898  
899  
900  
901  
902  
903  
904  
905  
906  
907  
908  
909  
910  
911  
912  
913  
914  
915  
916  
917  
918  
919  
920  
921  
922  
923  
924  
925  
926  
927  
928  
929  
930  
931  
932  
933  
934  
935  
936  
937  
938  
939  
940  
941  
942  
943  
944  
945  
946  
947  
948  
949  
950  
951  
952  
953  
954  
955  
956  
957  
958  
959  
960  
961  
962  
963  
964  
965  
966  
967  
968  
969  
970  
971  
972  
973  
974  
975  
976  
977  
978  
979  
980  
981  
982  
983  
984  
985  
986  
987  
988  
989  
990  
991  
992  
993  
994  
995  
996  
997  
998  
999  
1000

### 3.2 XRD characterisation

To further investigate the phase transformation process, XRD analysis was used to characterise the phases of the precursors and samples calcined at temperatures of at 200–800 °C for 2 h. Figure 3 shows the scanned XRD spectra of the precursor and zirconia powders prepared at varying calcination temperatures. Figure 3 shows that both the precursor and the sample calcined at 200 °C were amorphous. The

1 characteristic peaks for the tetragonal zirconia phase ( $t\text{-ZrO}_2$ ) were observed when the sample was calcined  
2  
3 at 400 °C, the  $t\text{-ZrO}_2$  diffraction peak became more intense, and its crystallisation was favored when the  
4  
5 sample was calcined at 800 °C. The average grain sizes calculated using Scherrer's equation were 18.6,  
6  
7 23.3, and 28.7 nm for samples calcined at temperatures of 400–800 °C, respectively, which indicated that  
8  
9 the calcination temperature was positively correlated with the grain size of the powders. In finding the  
10  
11 average particle size, XRD data from large angle diffraction was used, taking the strongest and most stable  
12  
13 diffraction peaks where they can be found. However, the peaks were sharper and had smaller full widths at  
14  
15 half maxima (FWHMs) as the calcination temperature increased, and the best crystallinity for the zirconia  
16  
17 powder sample was observed at 800 °C.  
18  
19  
20  
21  
22  
23  
24

### 25 3.3 Raman characterisation

26  
27 Raman spectroscopy is an effective way to distinguish the zirconia crystalline form. The tetragonal  
28  
29 phase of zirconia has six Raman active vibrational modes ( $A_{1g}+2B_{1g}+3E_g$ ):  $A_{1g}^+$ : 600  $\text{cm}^{-1}$  (very weak),  $B_{1g}$ :  
30  
31 147 and 315  $\text{cm}^{-1}$ ,  $E_g$ : 269, 459, and 643  $\text{cm}^{-1}$ . Theoretically, the cubic phase has only one Raman active  
32  
33 vibrational mode, typically observed as a broad spectral peak from 530 to 670  $\text{cm}^{-1}$  [38]. The monoclinic  
34  
35 phase has 18 Raman active vibrational modes: ( $9A_g+9B_g$ ) and the following vibration spectral peaks can  
36  
37 generally be observed:  $A_g$ : 176, 187, 300, 475, 558, 635, and 760  $\text{cm}^{-1}$ ,  $B_g$ : 220, 333, 344, 380, 510, 536,  
38  
39 and 613  $\text{cm}^{-1}$ . For further differentiation, Raman spectroscopy was performed on the obtained zirconia  
40  
41 nanoparticle samples, and Raman spectra are shown in Fig. 4(a). The zirconia samples showed a small  
42  
43 number of weak vibrational peaks associated with the monoclinic phase, while vibrational peaks  
44  
45 corresponding to the tetragonal phase were observed at 146, 260, 318, 464, and 642  $\text{cm}^{-1}$ , and no broad  
46  
47 peaks were observed in the cubic phase wavelength range of 530–670  $\text{cm}^{-1}$ . Thus, it was confirmed that the  
48  
49 obtained Mg-Y/ZrO<sub>2</sub> nanoparticles were mixed crystals with a large amount of the tetragonal zirconia  
50  
51  
52  
53  
54  
55  
56  
57  
58  
59  
60  
61  
62  
63  
64  
65

1 phase and a small of the monoclinic zirconia (*m*-ZrO<sub>2</sub>) phase. Moreover, the *t*-ZrO<sub>2</sub> phase vibrational peak  
2  
3 intensity gradually showed a positive relationship with the calcination temperature, which further  
4  
5 confirmed that the crystallinity of the sample reached a maximum after calcination at 800 °C, where the  
6  
7 transformation from the amorphous phase to the tetragonal phase was nearly complete.  
8  
9

10  
11 The original Raman spectra were fitted with multiple Gaussian peaks using the Origin software. The  
12  
13 relationship between the calcination temperature and crystalline phase composition of the powders was  
14  
15 investigated in detail based on characteristic spectral information, such as the position, intensity, area, and  
16  
17 FWHM of the Gaussian peaks. Figures 4(b)–(d) show the fitted curves of Raman spectra for samples  
18  
19 calcined at temperatures of 400–800 °C, respectively. With increasing calcination temperature, the peak  
20  
21 areas of the characteristic Raman peak positions gradually increased, whereas the FWHM gradually  
22  
23 decreased. Furthermore, since crystallinity is negatively correlated with FWHM, it was concluded that  
24  
25 crystallinity gradually increased with increasing calcination temperature. Moreover, maintaining the  
26  
27 precursor at a calcination temperature of 800 °C for 2 h was sufficient to achieve the best crystallinity in  
28  
29 this study. The Raman results were consistent with the XRD results.  
30  
31  
32  
33  
34  
35  
36  
37  
38

### 39 **3.4 FTIR characterization**

40  
41 The effects of co-doping magnesium and yttrium on the surface chemical structure of zirconia  
42  
43 powders were investigated by FTIR measurements of samples prepared at various calcination temperatures.  
44  
45 As shown in the first red curve of Fig. 5, five characteristic FTIR peaks were detected in the prepared  
46  
47 precursor powders at 3411.67, 1590.48, 1352.05, 1063.86, and 422.30 cm<sup>-1</sup>. Specifically, the characteristic  
48  
49 absorption peaks of Zr-O, Zr=O, and Zr-O-Zr bonds appeared at wavelengths of 1352.05, 1063.86, and  
50  
51 600–650 cm<sup>-1</sup>, respectively, which confirmed the presence of zirconia. Highly pure water was used as the  
52  
53 medium in the co-precipitation experiments; therefore, strong Zr-OH and O-H vibrational absorption peaks  
54  
55  
56  
57  
58  
59  
60  
61  
62  
63  
64  
65

1 were observed at 3411.67 and 1590.48  $\text{cm}^{-1}$ , respectively. Thus, the hydrophilic nature of the O-H bond  
2  
3 facilitated the dispersion of zirconium oxide in water during the preparation process. Because no surface  
4  
5 modifier was added during the preparation process, no other peaks were present in the FTIR spectrum of  
6  
7 the precursors.  
8  
9

10  
11 Furthermore, based on the FTIR spectra of the precursor and powders prepared at calcination  
12  
13 temperatures of 200–800  $^{\circ}\text{C}$ , it was possible to compare the characteristic peak at 422.30  $\text{cm}^{-1}$ , which  
14  
15 increased and shifted to a higher wavelength with a Doppler shift (blue shift) with increasing calcination  
16  
17 temperature. This phenomenon was explained by the exchange of heat with an increase in calcination  
18  
19 temperature, which led to a phase transformation to form crystalline particles, followed by the formation of  
20  
21 the pure tetragonal phase in the final calcined Mg-Y/ZrO<sub>2</sub> sample.  
22  
23  
24  
25  
26

### 27 **3.5 BET characterisation**

28  
29 A specific surface area tester was used to analyse the nitrogen adsorption-desorption curves. Powder  
30  
31 samples were dried at a constant temperature of 150  $^{\circ}\text{C}$  for 6 h and tested at -196  $^{\circ}\text{C}$  in liquid nitrogen  
32  
33 atmosphere. The pore size distribution (PSD) curves of the powder samples were calculated using the  
34  
35 Barrett–Joyner–Halenda (BJH) algorithm, and the specific surface areas of the powder samples were  
36  
37 obtained using the BET algorithm.  
38  
39  
40  
41  
42  
43

44  
45 Figure 6 shows the nitrogen adsorption-desorption curves and PSD curves for the precursors and  
46  
47 powder samples calcined at temperatures of 200–800  $^{\circ}\text{C}$ . Figure 6(a) shows that the adsorption-desorption  
48  
49 curves of the precursor calcined at temperatures of 200 and 400  $^{\circ}\text{C}$  had a distinct inflection (point A) at low  
50  
51  $P/P_0$ , which is the initial steep region of the isotherm. Inflection point A indicates that the adsorption  
52  
53 corresponding to the monolayer reached the maximum saturation adsorption capacity. The second  
54  
55 molecular layer started to accumulate by adsorption as the relative pressure increased. At the saturated  
56  
57  
58  
59  
60  
61  
62  
63  
64  
65

1 vapour pressure, the number of adsorbed molecular layers is unlimited; thus, these powder samples  
2  
3 exhibited a type II isotherm (also called type S). In contrast, the adsorption-desorption isotherms of powder  
4  
5 samplers calcines at a temperature of 600 and 800 °C exhibited the typical type IV isotherm, which curves  
6  
7 convexly upwards in the low  $P/P_0$  region. Conversely, in the higher  $P/P_0$  region, the isotherm increases  
8  
9 sharply because of capillary coalescence of the adsorbate. Subsequently, adsorption occurs only on the  
10  
11 external surface, and the curve becomes flat when all the pores coalesce. At relative pressures close to 1,  
12  
13 adsorption occurs on the larger pores and the curve increases. Because of the occurrence of capillary  
14  
15 coalescence, hysteresis is observed in the area, and the isotherm obtained during desorption disagrees with  
16  
17 the adsorption branch of the isotherm. The former isotherm is higher, producing an adsorption hysteresis,  
18  
19 which causes the back-lag cycle. According to the latest IUPAC classification, the saturation adsorption  
20  
21 plateau of the H3 type hysteresis loop was absent in the isotherm of the powder sample calcined at a  
22  
23 temperature of 600 °C, which indicated a remarkably irregular pore structure. The H2 type hysteresis loop  
24  
25 observed for the powder sample prepared at a calcination temperature of 800 °C had a saturation adsorption  
26  
27 plateau in the isotherm, which indicated a more uniform pore size distribution.

28  
29  
30  
31  
32  
33  
34  
35  
36  
37  
38  
39 The PSD curves shown in Fig. 6(b) indicate that the most accessible pore size was 12.216 nm, which  
40  
41 was observed for the powder sample prepared at a calcination temperature of 800 °C. The BET analysis  
42  
43 showed that the specific surface area of zirconia nanopowders has a negative relationship with the  
44  
45 calcination temperature, the minimum particle size was received at the calcined temperature of 200 °C.  
46  
47 However, we have noticed that hard agglomerates were formed in the sample prepared with a calcined  
48  
49 temperature of 200 °C because of the great surface activity of the sample. Whilst, samples calcined at  
50  
51 800 °C have a specific surface area of 13.249 m<sup>2</sup>/g, leading to a more uniform particle size distribution,  
52  
53  
54  
55  
56  
57  
58  
59  
60  
61  
62  
63  
64  
65

high sphericity, and lower surface energy, which makes them more favorable for subsequent applications [39-42].

### 3.6 SEM characterization

The SEM results showed the distribution and morphology of zirconia clusters. Samples were tested by dropping a 50 wt.% mass fraction of the zirconia cluster dispersion onto a silicon wafer, followed by drying under ambient conditions. Before SEM analysis, the samples were subjected to gold plating to impart electrical conductivity.

Figures 7(a)–(d) show the SEM images of the Mg-Y/ZrO<sub>2</sub> nanoparticles obtained by calcination at temperatures of 200–800 °C, at 200 000 times magnification using high-magnification electron microscopy. A comparison of the four SEM micrographs shows that the calcination temperature was positively correlated with the nano-zirconia particle diameter. The nano Mg-Y/ZrO<sub>2</sub> powder particles prepared at a calcination temperature of 200 °C were small but irregularly arranged, and intermolecular forces led to distinct agglomeration. At calcination temperatures of 400–600 °C, the nano Mg-Y/ZrO<sub>2</sub> powder particles grew in size gradually, and the quasi-spherical morphology was gradually enhanced. At a calcination temperature of 800 °C, particle agglomeration was absent in the prepared nano Mg-Y/ZrO<sub>2</sub> powder, and the particle morphology was sphere-like with a more uniform particle distribution (shown in Fig. 7(d)). Therefore, a calcination temperature of 800 °C was the optimal temperature for stabilising the crystal shape of nano Mg-Y/ZrO<sub>2</sub> powder and maintaining a good dispersion.

## 4. Conclusion

In this study, a co-precipitation process was proposed to synthesise Mg-Y/ZrO<sub>2</sub> nanopowders with a regular spherical morphology, good crystallisation, uniform distribution, and ultrafine diameter. The

1 obtained samples were characterised by TG-DSC, XRD, Raman, FTIR, nitrogen adsorption using BET  
2  
3 theory, TEM, and FESEM. The main conclusions are as follows:  
4

5  
6 (1) Effect of calcination temperature on crystallinity: Both the precursors and the samples calcined at  
7  
8 200 °C were amorphous. The transformation of the precursor was initiated at a calcination temperature of  
9  
10 292 °C. The characteristic peaks of the tetragonal zirconia phase were observed at calcination temperatures  
11  
12 of 500 °C; the tetragonal zirconia diffraction peak increased and its crystallisation was favoured at a  
13  
14 calcination temperature of 800 °C.  
15  
16  
17

18  
19 (2) Effect of calcination temperature on dispersibility: The specific surface area of the Mg-Y/ZrO<sub>2</sub>  
20  
21 nanoparticles was negatively correlated with calcination temperature. The elevated heat reduced the surface  
22  
23 energy of the nano-zirconia powder, and consequently resulted in a good powder dispersion.  
24  
25  
26

27  
28 (3) The optimised synthesis conditions for the preparation of Mg-Y/ZrO<sub>2</sub> nanopowders were: 6 h of  
29  
30 high-energy planetary grinding, calcination at 800 °C in an electric furnace. Under optimum conditions, the  
31  
32 average diameter of the prepared particles was 28.7 nm. The process will enrich the research data in  
33  
34 literature on the controllable preparation of MgO-Y<sub>2</sub>O<sub>3</sub> co-stabilized ZrO<sub>2</sub> nanopowders using the  
35  
36 co-precipitation method.  
37  
38  
39  
40  
41  
42  
43

#### 44 **Acknowledgments**

45  
46  
47 Financial support from the National Natural Science Foundation of China (Grant No.  
48  
49 51764052) and Innovative Research Team (in Science and Technology) in University of  
50  
51 Yunnan Province.  
52  
53  
54  
55  
56  
57  
58  
59  
60  
61  
62  
63  
64  
65

## References

- [1] E. Roitero, F. Lasserre, M. Anglada, F. Mücklich, E. JiménezPiqué, A parametric study of laser interference surface patterning of dental zirconia: Effects of laser parameters on topography and surface quality, *Dent. Mater.* 33 (1) (2017) e28-e38.  
<https://doi.org/10.1016/j.dental.2016.09.040>.
- [2] S.M. Yong, D.H. Choi, K. Lee, S.Y. Ko, D.I. Cheong, Y.J. Park, S.I. Go, Study on carbon contamination and carboxylate group formation in  $Y_2O_3$ -MgO nanocomposites fabricated by spark plasma sintering, *J. Eur. Ceram. Soc.* 40 (3) (2019) 847-851.  
<https://doi.org/10.1016/j.jeurceramsoc.2019.10.035>.
- [3] J. Wang, L. Zhang, D. Chen, E.H. Jordan, M. Gell,  $Y_2O_3$ -MgO-ZrO<sub>2</sub> infrared transparent ceramic nanocomposites, *J. Am. Ceram. Soc.* 95 (3) (2012) 1033-1037.  
<https://doi.org/10.1111/j.1551-2916.2011.04928.x>.
- [4] J. Wen, T. Zhu, Z. Xie, W. Cao, W. Liu, A strategy to obtain a high-density and high-strength zirconia ceramic via ceramic injection molding by the modification of oleic acid, *Int. J. Min. Met. Mater.* 24 (6) (2017) 718-725. <https://doi.org/10.1007/s12613-017-1455-9>.
- [5] E. Jiménez-Piqué, A. Ramos, J.A. Muñoz-Tabares, A. Hatton, F. Soldera, F. Mücklich, M. Anglada, Focused ion beam tomography of zirconia degraded under hydrothermal conditions, *J. Eur. Ceram. Soc.* 32 (10) (2012) 2129-2136. <https://doi.org/10.1016/j.jeurceramsoc.2012.02.011>.
- [6] N. Wu, X.D. Li, J.G. Li, Q. Zhu, X.D. Sun, Fabrication of  $Gd_2O_3$  - MgO nanocomposite optical ceramics with varied crystallographic modifications of  $Gd_2O_3$  constituent, *J. Am. Ceram. Soc.* 101 (11) (2018) 4887-4891. <https://doi.org/10.1111/jace.15884>.
- [7] L.H. Liu, K.J. Morita, T.S. Suzuki, B.N. Kim, Synthesis of highly-infrared transparent  $Y_2O_3$ -MgO nanocomposites by colloidal technique and SPS, *Ceram. Int.* 46 (9) (2020) 13669-13676.  
<https://doi.org/10.1016/j.ceramint.2020.02.153>.
- [8] N. Safronova, O. Kryzhanovska, M. Dobrotvorska, A. Balabanov, A. Tolmachev, R. Yavetskiy, S. Parkhomenko, R.Y. Brodskii, V. Baumer, D.Y. Kosyanov, Influence of sintering temperature on structural and optical properties of  $Y_2O_3$ -MgO composite SPS ceramics, *Ceram. Int.* 46 (5) (2020) 6537-6543.  
<https://doi.org/10.1016/j.ceramint.2019.11.137>.

- 1  
2  
3  
4  
5  
6  
7  
8  
9  
10  
11  
12  
13  
14  
15  
16  
17  
18  
19  
20  
21  
22  
23  
24  
25  
26  
27  
28  
29  
30  
31  
32  
33  
34  
35  
36  
37  
38  
39  
40  
41  
42  
43  
44  
45  
46  
47  
48  
49  
50  
51  
52  
53  
54  
55  
56  
57  
58  
59  
60  
61  
62  
63  
64  
65
- [9] G. Urruth, D. Maury, C. Voisin, V. Baylac, D. Grossin, Powder bed selective laser processing (sintering/melting) of Yttrium Stabilized Zirconia using carbon-based material (TiC) as absorbance enhancer, *J. Eur. Ceram. Soc.* 42 (5) (2022) 2381-2390.  
<https://doi.org/10.1016/j.jeurceramsoc.2021.12.042>.
- [10] Z. Zeng, Y. Liu, Y. Zhang, Z. Zhou, X. Liu, Ferroelastic domain switching toughening in Ce-Y-La co-stabilized zirconia ceramics obtained from coated starting powders, *J. Alloy. Compd.* 820 (2020) 153177.  
<https://doi.org/10.1016/j.jallcom.2019.153177>.
- [11] J.H. Cheng, C.G. Tian, J. Yang, J.B. He, Electrical and mechanical properties of Sm<sub>2</sub>O<sub>3</sub> doped Y-TZP electrolyte ceramics, *Ceram. Int.* 44 (14) (2018) 17033-17037.  
<https://doi.org/10.1016/j.ceramint.2018.06.146>.
- [12] H. Nahor, Y. Kauffmann, W.D. Kaplan, The Cr-Doped Ni-YSZ (111) interface: Segregation, oxidation and the Ni equilibrium crystal shape, *Acta. Mater.* 166 (2019) 28-36.  
<https://doi.org/10.1016/j.actamat.2018.12.023>.
- [13] Y. Ling, X. Hao, Y. Gui, H. Qiu, Q. Li, H. Zheng, M. Omran, L. Gao, J. Chen, G. Chen, Stability properties and microstructure properties of microwave-sintered CeO<sub>2</sub> doped zirconia ceramics, *Ceram. Int.* 47 (20) (2021) 28210-28217. <https://doi.org/10.1016/j.ceramint.2021.06.234>.
- [14] N. Li, D. An, Z.Z. Yi, N.T. Yu, Z.P. Xie, Synthesis of 1Y6Ce-ZrO<sub>2</sub> nanoparticles with excellent sintering performance via novel Sol-Gel-Flux method, *Ceram. Int.* 48 (2) (2021) 2637-2644.  
<https://doi.org/10.1016/j.ceramint.2021.10.047>.
- [15] D.S. Kim, W.C. Kim, J.K. Lee, Effect of solid loading on the sintered properties of 3 mol% yttria-stabilized tetragonal zirconia polycrystals (3Y-TZP) ceramics via slip casting, *J. Nanosci. Nanotechno.* 19 (10) (2019) 6383-6386. <https://doi.org/10.1166/jnn.2019.17045>.
- [16] Y.Q. Ling, Q.N. Li, H.W. Zheng, M. Omran, L. Gao, J. Chen, G. Chen, Optimisation on the stability of CaO-doped partially stabilised zirconia by microwave heating, *Ceram. Int.* 47 (6) (2021) 8067-8074.  
<https://doi.org/10.1016/j.ceramint.2020.11.161>.
- [17] T.P. Wen, L. Yuan, T. Liu, Q.Y. Sun, E.D. Jin, C. Tian, J.K. Yu, Enhanced ionic conductivity and thermal shock resistance of MgO stabilized ZrO<sub>2</sub> doped with Y<sub>2</sub>O<sub>3</sub>, *Ceram. Int.* 46 (12) (2020) 19835-19842. <https://doi.org/10.1016/j.ceramint.2020.05.038>.

- 1  
2 [18] H.Y. Abed, M. Almasi-Kashi, S.A. Zaidan, Effect grain size on physical properties of  
3 (Y<sub>2</sub>O<sub>3</sub>-ZrO<sub>2</sub>-MgO-Al<sub>2</sub>O<sub>3</sub>) system, J. Phys.: Conf. Ser. 1178 (1) (2019) 012004.  
4 <https://doi.org/10.1088/1742-6596/1178/1/012004>.  
5
- 6 [19] J.L. Vazquez-Arce, H. Tiznado, R. Kirchheim, Onset of electronic conductivity in nanometer thick  
7 films of yttria stabilized zirconia (YSZ) at high electric fields, Acta Mater. 229 (2022) 117826.  
8 <https://doi.org/10.1016/j.actamat.2022.117826>.  
9
- 10 [20] N. Li, N.T. Yu, Z.Z. Yi, D. An, Z.P. Xie. CeO<sub>2</sub>-stabilised ZrO<sub>2</sub> nanoparticles with excellent sintering  
11 performances synthesized by sol-gel-flux method, J. Eur. Ceram. Soc. (2021).  
12 <https://doi.org/10.1016/j.jeurceramsoc.2021.12.012>.  
13
- 14 [21] M. Rad, S. Borhani, M. Moradi, V. Safarifard, Tuning the crystallinity of ZrO<sub>2</sub> nanostructures derived  
15 from thermolysis of Zr-based aspartic acid/succinic acid MOFs for energy storage application, Physica E.  
16 134 (2021) 114921. <https://doi.org/10.1016/j.physe.2021.114921>.  
17
- 18 [22] Z. Dong, Z. Ma, L. Yu, Y. Liu, Achieving high strength and ductility in ODS-W alloy by employing  
19 oxide@ W core-shell nanopowder as precursor, Nat. Commun. 12 (1) (2021) 1-10.  
20 <https://doi.org/10.1038/s41467-021-25283-2>.  
21
- 22 [23] P.T. Chung, S.H. Chiou, C.Y. Tseng, A.S.T. Chiang, Preparation and evaluation of a  
23 zirconia/oligosiloxane nanocomposite for LED encapsulation, ACS. Appl. Mater. Inter. 8(15) (2016)  
24 9986-9993. <https://doi.org/10.1021/acsami.6b02082>.  
25
- 26 [24] Y. Wei, Z. Zhao, J. Jiao, J. Liu, A. Duan, G. Jiang, Preparation of ultrafine Ce-based oxide  
27 nanoparticles and their catalytic performances for diesel soot combustion, J. Rare Earth. 32 (2) (2014)  
28 124-130. [https://doi.org/10.1016/s1002-0721\(14\)60041-7](https://doi.org/10.1016/s1002-0721(14)60041-7).  
29
- 30 [25] X. He, Z. Wang, D. Wang, F. Yang, R. Tang, J. Wang, Y. Pu, J. Chen, Sub-kilogram-scale synthesis of  
31 highly dispersible zirconia nanoparticles for hybrid optical resins, Appl. Surf. Sci. 491 (2019) 505-516.  
32 <https://doi.org/10.1016/j.apsusc.2019.06.187>.  
33
- 34 [26] K. Kosai, J. Yan, Effects of cyclic loading on subsurface microstructural changes of zirconia  
35 polycrystals in nanoscale mechanical processing, Int. J. Mach. Tool. Manu. 159 (2020) 103626.  
36 <https://doi.org/10.1016/j.ijmachtools.2020.103626>.  
37  
38  
39  
40  
41  
42  
43  
44  
45  
46  
47  
48  
49  
50  
51  
52  
53  
54  
55  
56  
57  
58  
59  
60  
61  
62  
63  
64  
65

- 1  
2 [27] L. Liu, S. Wang, B. Zhang, G. Jiang, J. Yang, Y. Li, W. Liu, J. Wang, W. Kong, From modification to  
3 mechanism: Supercritical hydrothermal synthesis of nano-zirconia, *Ceram. Int.* 48 (4) (2022) 4401-4423.  
4 <https://doi.org/10.1016/j.ceramint.2021.11.028>.  
5  
6  
7 [28] Y. Chang, S. Dong, H. Wang, K. Du, Q. Zhu, P. Luo, Synthesis of monodisperse spherical nanometer  
8  
9  
10  $ZrO_2$  ( $Y_2O_3$ ) powders via the coupling route of w/o emulsion with urea homogenous precipitation, *Mater.*  
11  
12 *Res. Bull.* 47 (3) (2012) 527-531. <https://doi.org/10.1016/j.materresbull.2011.12.055>.  
13  
14  
15 [29] S.M. Dezfuli, A. Shanaghi, S. Baghshahi, Effect of  $Al_2O_3$  and  $Y_2O_3$  on the corrosion behavior of  
16  
17  
18  $ZrO_2$ -benzotriazole nanostructured coatings applied on AA2024 via a sol-gel method, *Int. J. Min. Met.*  
19  
20  
21 *Mater.* 25 (11) (2018) 1344-1353. <https://doi.org/10.1007/s12613-018-1688-2>.  
22  
23 [30] S.J. Hao, C. Wang, T.L. Liu, Z.M. Mao, Z.Q. Mao, J.L. Wang, Fabrication of nanoscale yttria  
24  
25 stabilized zirconia for solid oxide fuel cell, *Int. J. Hydrogen Energ.* 42 (50) (2017) 29949-29959.  
26  
27 <https://doi.org/10.1016/j.ijhydene.2017.08.143>.  
28  
29 [31] J.J. Xia, H.R. Guo, M.Z. Cheng, C.Y. Chen, M.K. Wang, Y. Xiang, T.S. Li, E. Traversa, Electrospun  
30  
31 zirconia nanofibers for enhancing the electrochemical synthesis of ammonia by artificial nitrogen fixation,  
32  
33  
34 *J. Mater. Chem. A* 9 (4) (2021) 2145-2151.  
35  
36 <https://doi.org/10.1039/D0TA08089F>.  
37  
38 [32] K. VanEvery, M.J.M. Krane, R.W. Trice, Parametric study of suspension plasma spray processing  
39  
40 parameters on coating microstructures manufactured from nanoscale yttria-stabilized zirconia, *Surf. Coat.*  
41  
42 *Tech.* 206 (8-9) (2012) 2464-2473.  
43  
44 <https://doi.org/10.1016/j.surfcoat.2011.10.051>.  
45  
46 [33] B. Tyagi, K. Sidhpuria, B. Shaik, R.V. Jasra, Synthesis of nanocrystalline zirconia using sol-gel and  
47  
48 precipitation techniques, *Ind. Eng. Chem. Res.* 45 (25) (2006) 8643-8650.  
49  
50 <https://doi.org/10.1021/ie060519p>.  
51  
52 [34] M. Meepho, D. Wattasiriwech, S. Wattanasiriwech, P. Angwattana, Influence of reaction medium on  
53  
54 formation of nanocrystalline YSZ prepared by conventional and modified solvothermal process, *Energy*  
55  
56 *Procedia* 9 (1) (2011) 545-552. <https://doi.org/10.1016/j.egypro.2011.09.063>.  
57  
58  
59  
60  
61  
62  
63  
64  
65

- 1 [35] G. Roncallo, G. Cacciamani, E. Vacchieri, M. Ilatovskaia, I. Saenko, O. Fabrichnaya, Thermodynamic  
2 modeling and experimental investigation of the MgO - Y<sub>2</sub>O<sub>3</sub> - ZrO<sub>2</sub> system, *J. Am. Ceram. Soc.* 103 (9)  
3  
4  
5  
6 (2020) 5337-5353. <https://doi.org/10.1111/jace.17224>.
- 7 [36] J. Santoyo-Salazar, G. Gonzalez, J.A. Ascencio, J. Tartaj-Salvador, J.A. Chávez-Carvayar, Novel  
8 yttria-stabilised zirconia-alumina tetragonal phase obtained by co-precipitation, *J. Cryst. Growth* 290 (1)  
9  
10  
11  
12 (2006) 307-312. <https://doi.org/10.1016/j.jcrysgro.2006.01.032>.
- 13 [37] Y.W. Hsu, K.H. Yang, K.M. Chang, S.W. Yeh, M.C. Wang, Synthesis and crystallisation behavior of 3  
14 mol% yttria stabilized tetragonal zirconia polycrystals (3Y-TZP) nanosized powders prepared using a  
15 simple co-precipitation process, *J. Alloy. Compd.* 509 (24) (2011) 6864-6870.  
16  
17  
18  
19  
20  
21 <https://doi.org/10.1016/j.jallcom.2011.03.162>.
- 22 [38] X. He, Z. Wang, Y. Pu, D. Wang, R. Tang, S. Cui, J. Wang, J. Chen, High-gravity-assisted scalable  
23 synthesis of zirconia nanodispersion for light emitting diodes encapsulation with enhanced light extraction  
24 efficiency, *Chem. Eng. Sci.* 195 (2019) 1-10. <https://doi.org/10.1016/j.ces.2018.11.036>.
- 25  
26  
27  
28  
29 [39] Q. Feng, X. Ma, Q. Yan, C. Ge, Preparation of soft-agglomerated nano-sized ceramic powders by  
30 sol-gel combustion process, *Mat. Sci. Eng. B-ADV* 2009, 162(1): 53-58.  
31  
32  
33  
34 <https://doi.org/10.1016/j.mseb.2009.02.007>.
- 35 [40] S. Salem, S. Jazayeri, F. Bondioli, A. Allahverdia, M. Shirvania, Characterizing thermal behavior of  
36 ceramic glaze containing nano-sized cobalt-aluminate pigment by hot stage microscopy, *Thermochim. acta*  
37  
38  
39  
40  
41 2011, 521(1-2): 191-196. <https://doi.org/10.1016/j.tca.2011.04.023>.
- 42 [41] H. Qiu, W. Huang, Y. Zhang, J. Chen, L. Gao, M. Omran, L. Nan, G. Chen, Preparation of nano-sized  
43 6MgO-2Y<sub>2</sub>O<sub>3</sub>-ZrO<sub>2</sub> powders by a combined co-precipitation and high energy ball milling process, *Ceram.*  
44  
45  
46  
47  
48  
49  
50  
51  
52  
53  
54  
55  
56  
57  
58  
59  
60  
61  
62  
63  
64  
65 Int. 2022. <https://doi.org/10.1016/j.ceramint.2022.03.207>.
- [42] Y. El Jabbar, H. Lakhliifi, R. El Ouatib, L. Er-Rakho, S. Guillemet-Fritsch, B. Durand, Preparation and  
characterisation of green nano-sized ceramic pigments with the spinel structure AB<sub>2</sub>O<sub>4</sub> (A= Co, Ni and B=  
Cr, Al). *Solid State Commun.* 2021, 334: 114394. <https://doi.org/10.1016/j.ssc.2021.114394>.

Table 1. Experimental drug specifications and manufacturer.

Name	Standards	Manufacturer
ZrOCl <sub>2</sub> ·8H <sub>2</sub> O	AR, ≥ 99.0%	Sinopharm Chemical Reagent Co. , LTD
MgCl <sub>2</sub> ·6H <sub>2</sub> O	AR, ≥ 98.0%	Sinopharm Chemical Reagent Co. , LTD
Y(NO <sub>3</sub> ) <sub>3</sub> ·6H <sub>2</sub> O	AR, ≥ 99.99%	Shanghai Aladdin Biochemical Technology Co. , LTD
NH <sub>3</sub> ·H <sub>2</sub> O	AR, 25–28%	Jiangsu Qiangsheng Functional Chemistry Co. , LTD
AgNO <sub>3</sub>	AR, 0.1000mol/L	Yida Technology Co. , LTD
CH <sub>3</sub> CH <sub>2</sub> OH	AR	Tianjin Zhiyuan Chemical Reagent Co. , LTD
UP H <sub>2</sub> O	18MΩ.cm	Laboratory homebrew

Table 2. Experimental instruments and equipment.

Name	Model
X-ray Diffraction	Bruker D8 Advance A25×
Renishaw Raman Microscope System	inVia
Field Emission Scanning Electron Microscopy	NOVA NANOSEM-450
Fourier Transform Infrared Spectroscopy	NICOLET-IS10, Nicolet, USA
Thermal Gravimetric Analyzer	NETZSCH STAA49F31
Brunner Emmet Teller	BELSORP-max II
Transmission Electron Microscopy	JEM-2100
Planetary Ball Mill	QM-3SP4

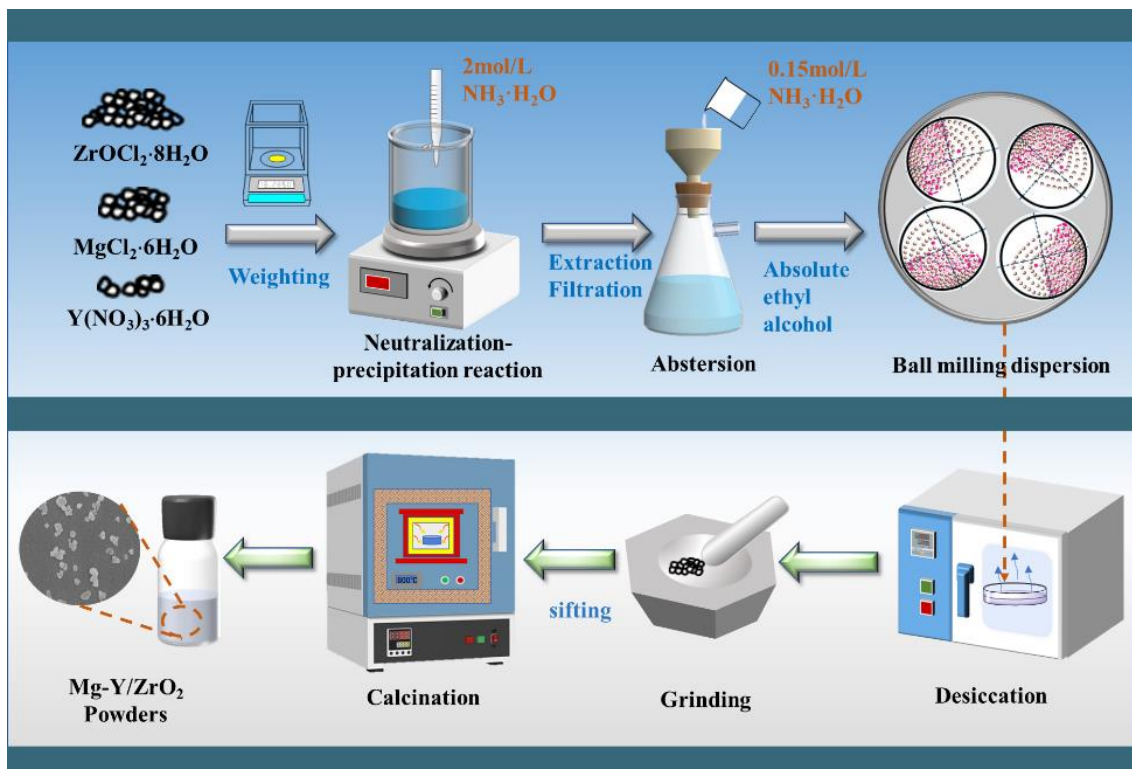


Fig. 1 Experimental flow diagram of the preparation of nanoscale *t*-Mg-Y/ZrO<sub>2</sub> samples using co-precipitation method.

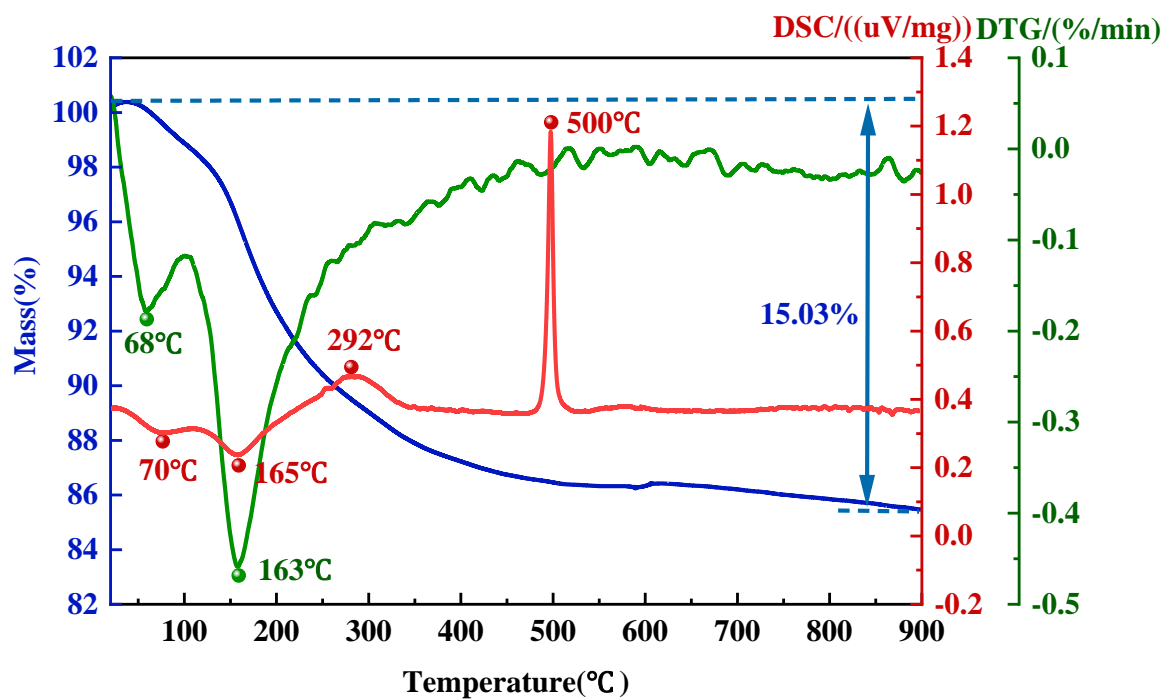


Fig. 2 TG-DSC curves of the precursor samples prepared by ball milling for 6 h.

1  
2  
3  
4  
5  
6  
7  
8  
9  
10  
11  
12  
13  
14  
15  
16  
17  
18  
19  
20  
21  
22  
23  
24  
25  
26  
27  
28  
29  
30  
31  
32  
33  
34  
35  
36  
37  
38  
39  
40  
41  
42  
43  
44  
45  
46  
47  
48  
49  
50  
51  
52  
53  
54  
55  
56  
57  
58  
59  
60  
61  
62  
63  
64  
65

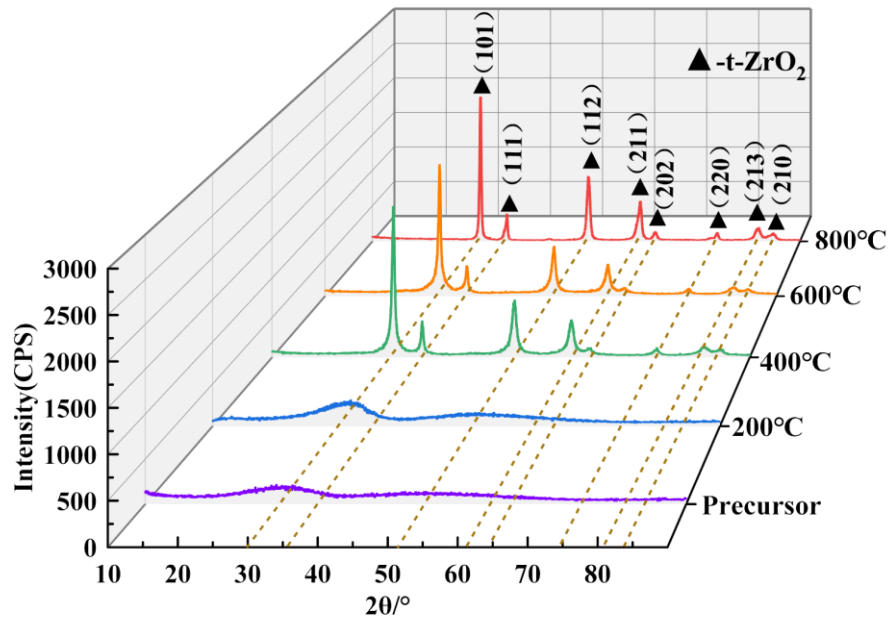


Fig. 3 XRD spectra of zirconia powders prepared under experimental conditions of precursors and calcination temperatures of 200–800 °C.

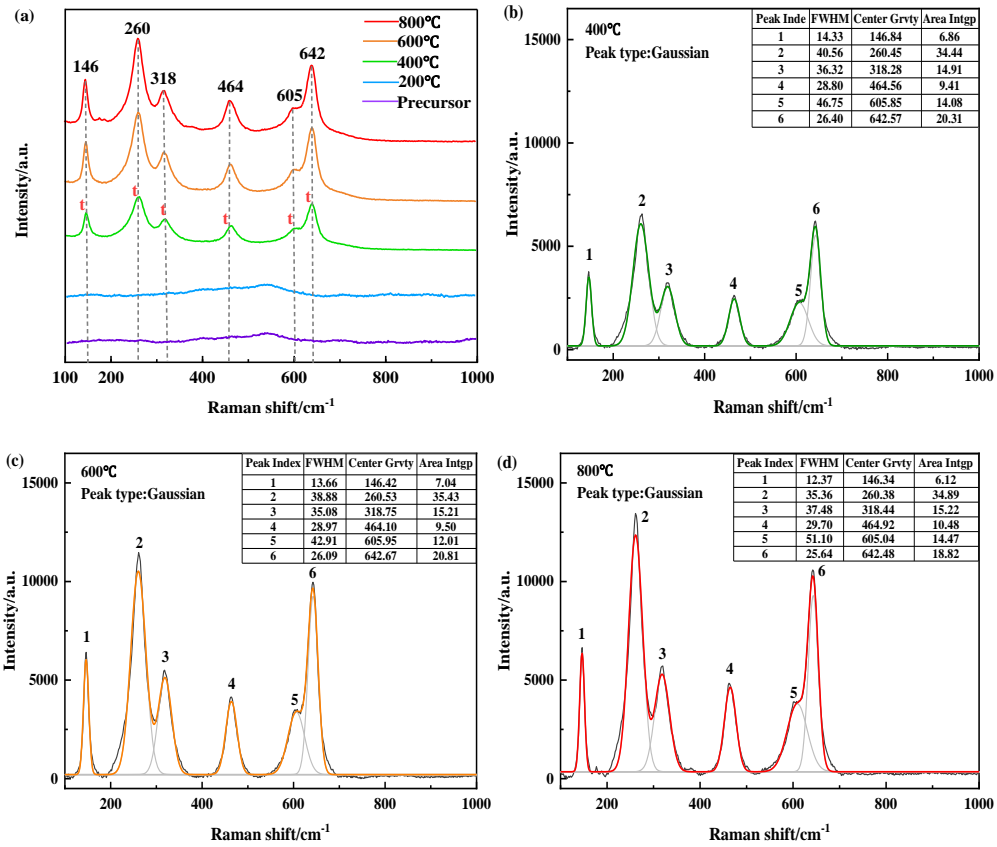


Fig. 4 (a) Raman spectra at different calcination temperatures. (b), (c), and (d) Gaussian fitted Raman curves at calcination temperatures of 400–800 °C.

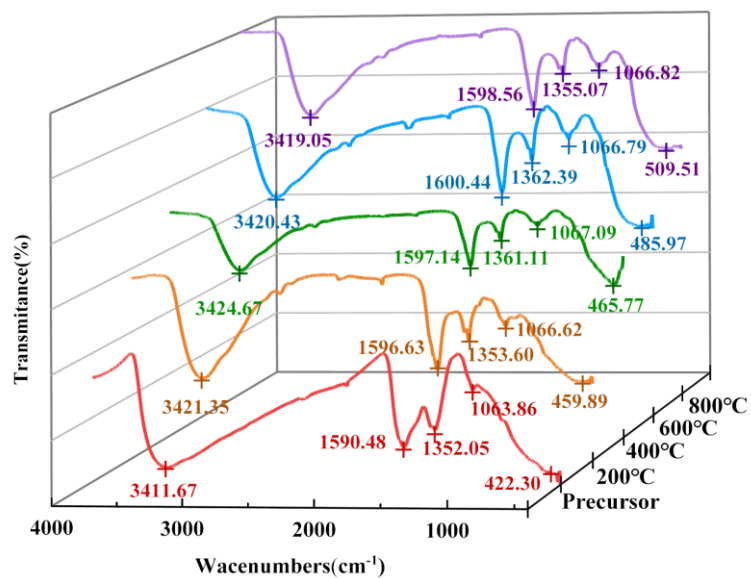


Fig. 5 FTIR spectra of precursors and zirconia nanopowders prepared at different calcination temperatures.

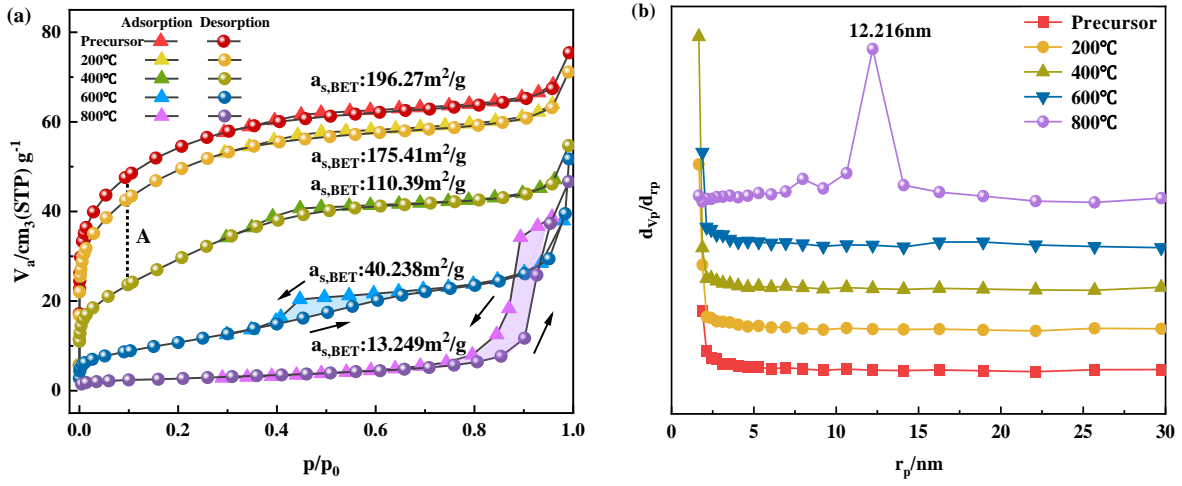


Fig. 6 Nitrogen adsorption-desorption curves and PSD curves of precursors and zirconia nanopowders prepared at calcination temperatures of 200–800 °C.

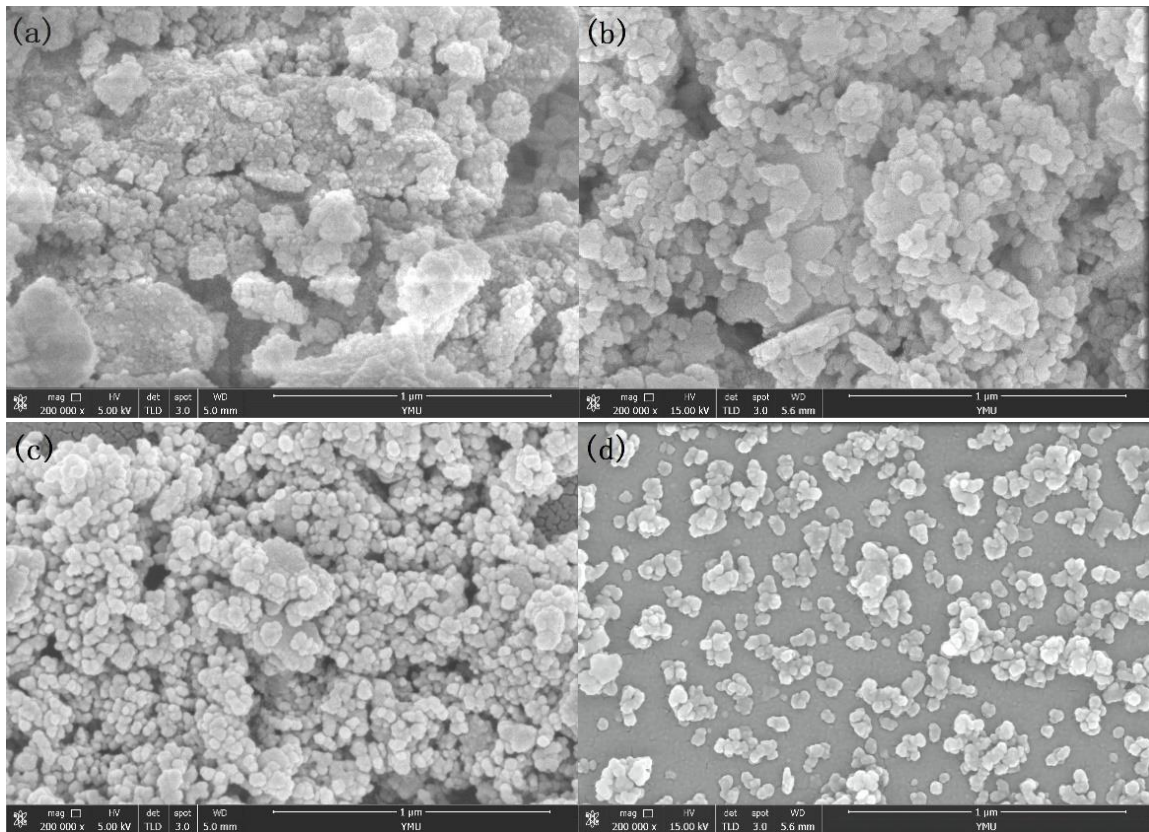


Fig. 7 (a)–(d) shows the SEM images of zirconia nanopowders obtained at different calcination temperatures of 200–800 °C.